Journal of Wind Engineering & Industrial Aerodynamics 243 (2023) 105606

Contents lists available at ScienceDirect

Journal of Wind Engineering & Industrial Aerodynamics

journal homepage: www.elsevier.com/locate/jweia

Stability analysis of two-dimensional flat solar trackers using aerodynamic derivatives at different heights above ground

Juan A. Cárdenas-Rondón *, Mikel Ogueta-Gutiérrez, Sebastián Franchini, Raul Manzanares-Bercial

Universidad Politécnica de Madrid. Instituto Universitario de Microgravedad "Ignacio Da Riva" (IDR/UPM), Plaza Cardenal Cisneros, 3, Madrid, 28040, Spain

ARTICLE INFO

Keywords:
Aerodynamic derivatives
Solar tracker
Wind tunnel
Aerodynamic instability

ABSTRACT

In this paper the aerodynamic stability of a flat-plate solar tracker under two-dimensional conditions is studied for different conditions of incident wind speed, U_∞, nominal angle of attack, $\alpha_n \in [-40°, 40°]$, and shaft height - chord ratio $H/B = 0.3,\ 0.4,\ 0.5,\ 0.6,\ 1$ and 2. The stability is studied through the analysis of the aerodynamic derivatives A_2^* and A_3^* whose behaviours as a function of U_∞ are presented for the H/B range studied. Two methods of obtaining the derivatives (one in the time domain and the other one in the frequency domain) are presented. A method for calculating the effective damping coefficient of the solar tracker, ξ^{eff}, as a function of the incident wind speed, U_∞, is presented. This method can be used for any solar tracker structural characteristics (J^{mech}, C^{mech} and K^{mech}). With this method, the critical speed, U_{crit}, can be determined by imposing the condition $\xi^{eff} = 0$. The method was validated experimentally using the results of two different experimental set-ups.

1. Introduction

Photovoltaic solar energy has become one of the most important sources of renewable energy today. Although there are various technologies for harnessing solar energy, one of the most widespread and efficient technologies for large-scale use is solar photovoltaic (PV) tracking systems. The use of this technology has become widespread in the solar industry in the form of plants or farms due to its ability to maximize electricity production. Examples of these plants, which consist of rows of single axis solar trackers oriented from north to south and mounted with photovoltaic solar panels, are shown in the photographs in Fig. 1. Photovoltaic panels, or solar panels, consist of an array of photovoltaic cells that generate electricity, from the light falling on them, by the photoelectric effect.

The solar panels are mounted on a structure that supports them and forms a solar tracker or array, as shown schematically in Fig. 2(left). The structure consists of a set of columns, a longitudinal axis or 'torque tube' and straps to which the solar panels are attached. Typically, a motor is installed in the centre of the row to drive the longitudinal axis, the straps attached to it, and the solar panels mounted on the straps. This mechanism orients the solar panels so that the solar radiation hits them as perpendicularly as possible (at the local solar elevation angle), as shown in Fig. 2(right). The swivel range is typically ±60°, measured from the zenith. Depending on the design, the length of the rows typically varies between 40 m and 60 m, with chords of approximately 2 m to 5 m.

To make the most of the energy, these plants are installed on large areas of land, with installed capacities ranging from tens to hundreds of megawatts. Because they require large areas of land, they are usually located in very open areas and exposed to the wind. For this reason, the effect of the wind is the most important factor to consider when calculating and designing these structures.

Since the mid-2010s, the solar industry has grown significantly, becoming more competitive and increasing the pressure to reduce the cost of these plants. According to the International Renewable Energy Agency (IRENA), the cost of the mechanical part of Photovoltaic Solar tracker (PST) represents between 15% and 35% of the total cost of these infrastructures (IRENA, 2022).

To reduce these costs, the PST industry has adapted its designs to optimize the structures and mechanisms of PSTs and make them more efficient overall. As a result, the overall stiffness of the PST has been progressively reduced, resulting in lower eigenfrequencies. In particular, the first eigenfrequencies in the torsional vibration mode along the "torque tube" make solar trackers sensitive to aeroelastic instabilities such as flutter and buffeting. Buffeting typically presents as low amplitude, high frequency oscillations, but enough to cause early fatigue in various elements of the solar tracker structure

* Corresponding author.
E-mail address: ja.cardenas@upm.es (J.A. Cárdenas-Rondón).

https://doi.org/10.1016/j.jweia.2023.105606
Received 18 May 2023; Received in revised form 4 November 2023; Accepted 4 November 2023
Available online 9 November 2023
0167-6105/© 2023 The Author(s). Published by Elsevier Ltd. This is an open access article under the CC BY-NC license (http://creativecommons.org/licenses/by-nc/4.0/).

List of Symbols

Greek symbols

α_n	Nominal angle of attack
α_{mean}^{eff}	Effective mean angle of attack
$\Delta\alpha$	Variation of the solar tracker angle of attack around its effective mean angle
$\Delta\alpha_0$	Initial displacement applied to the model above its equilibrium position
$\Delta\alpha_s$	Static deflection
$\Delta\ddot{\alpha}$	Acceleration of the solar tracker in rotation
$\Delta\dot{\alpha}$	Velocity of the solar tracker in rotation
ω	Angular velocity of the motion, $\omega = 2\pi f$
ω'	Spectrum frequency domain, $\omega = 2\pi f$
ω^*	Tentative angular velocity of the motion, $\omega = 2\pi f$
ω_n^{eff}	Effective natural angular velocity
ω_n^{mech}	Structural angular velocity
ρ	Air density
σ_{R^2}	Coefficient of determination standard deviation
ξ	Damping coefficient
ξ^{eff}	Effective damping coefficient
ξ^{mech}	Structural damping coefficient

Roman symbols

$\bar{a}$	Mean half-amplitude of a signal
$\bar{C}^{(\,)}$	$\bar{C}^{(\,)} = C^{(\,)}/J^{mech}$
$\bar{K}^{(\,)}$	$\bar{K}^{(\,)} = C^{(\,)}/J^{mech}$
a_0	Initial time of signal, a
A_2^*	Aerodynamic derivative related to "aerodynamic damping"
A_3^*	Aerodynamic derivative related to "aerodynamic stiffness"
A_p	Polynomial constant
B	Solar tracker chord
B_p	Polynomial constant
C^{aero}	Aerodynamic damping
C^{eff}	Effective damping
C^{mech}	Structural damping per unit length
C_m	Coefficient of moment around the rotation axis
C_p	Polynomial constant
$C_{m,\alpha}$	Slope of the static coefficient of moment curve with $\Delta\alpha$
D_p	Polynomial constant
E_p	Polynomial constant
f	Frequency of the motion
f_n^{eff}	Structural natural frequency
F_p	Polynomial constant
H	Height of the solar tracker axis
J	Number of measurements
j	Time instant, $j \in [0,\ J-1]$
J^{mech}	Inertia per unit length
k	Reduced frequency, $k = \omega B/U_\infty$
K^{aero}	Aerodynamic stiffness
K^{eff}	Effective stiffness
K^{mech}	Structural stiffness per unit length
L	Length of the solar tracker model
M_{se}	Unsteady self-excited aerodynamic moment
M_s	Steady aerodynamic moment
n	Logarithmic decrement
n^{eff}	Effective logarithmic decrement
n^{mech}	Structural logarithmic decrement
$P1$	Minimum value of A_2^*
$P2$	Reduced speed in which derivative A_2^* reaches zero again
R^2	Coefficient of determination
t	Time
t_m	Measurement time
U_∞	Free stream velocity
U_r	Reduced speed, $U_r = (2\pi U_\infty)/(\omega B) = (U_\infty)/(fB)$
U_{crit}	Critical speed
$U_{r,crit}$	Critical reduced speed
$X_{\omega'}$	Generic frequency domain discrete signal
x_j	Generic time domain discrete signal

Acronyms

DFT	Discrete Fourier Transform
FFT	Fast Fourier Transform
MDF	Middle Density Fibre
PST	Photovoltaic Solar Tracker
PV	Photovoltaic

(Simiu and Scanlan, 1996; Meseguer-Ruiz et al., 2013; Cárdenas-Rondón et al., 2022; Taylor and Browne, 2020; Browne et al., 2020). Flutter appears as high amplitude oscillations and frequencies close to the natural frequency of the structure. This instability can lead to catastrophic structural failure in a short period of time, as shown in the photographs in Fig. 3.

These instabilities can occur at relatively low wind speeds, even lower than the extreme speeds considered in the quasi-static design of structures. Therefore, the design of such structures is now determined by the dynamic behaviour of the structure rather than the quasi-static behaviour. This paper addresses the problem of flutter by presenting a methodology to predict the critical speed at which this instability occurs by determining the stability derivatives.

Observations made in the field, in wind tunnel tests and in numerical simulations (Martínez-García et al., 2021; Cheruku, 2022; Rohr et al., 2015) show that this instability is stall flutter. It is a phenomenon that involves the partial or complete separation of the flow periodically during oscillation. The essential characteristic of stall flutter is the nonlinear aerodynamic reaction to the motion of the structure. Therefore, this instability must be explained in terms of the nonlinear aerodynamic momentum (Cárdenas-Rondón et al., 2019; Li et al., 2016; Chen et al., 2022; Sisto, 2015).

Since the public reports of the occurrence of this instability in photovoltaic solar trackers is relatively recent, there is not much scientific literature that specifically addresses this problem. The first reference found on this phenomenon is the work of Rohr et al. (2015), in which a 2D analysis carried out with CFD is presented, coupled with a one-degree-of-freedom torsional dynamics solver, and a wind tunnel test of a reduced scale model. This study is carried out without considering the effect of the ground. The authors conclude that this phenomenon is caused by the coupling between the alternate release of vortices between the upper surface and the lower surface of the tracker and

Fig. 1. Single-axis photovoltaic solar tracker plants.

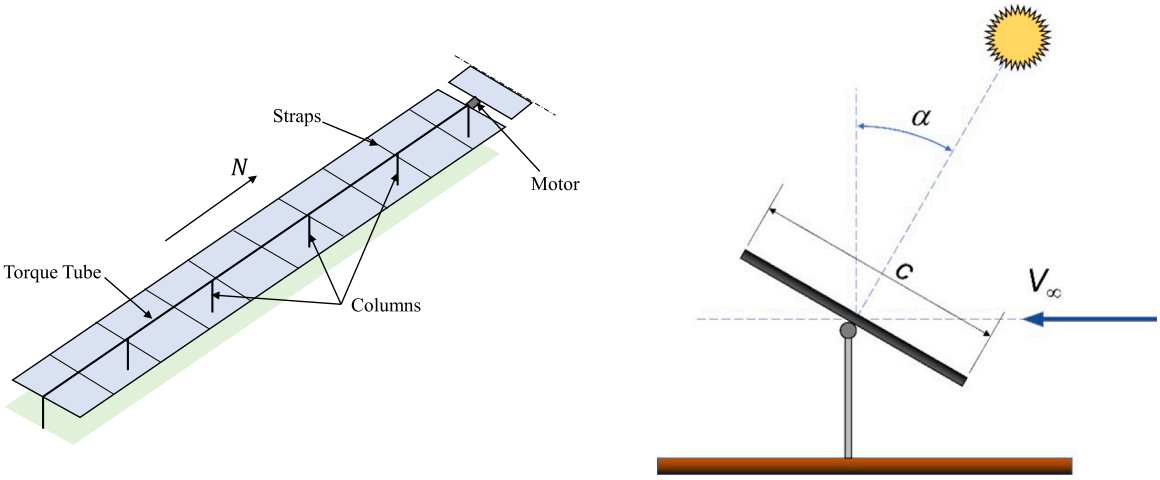

Fig. 2. Left: schematic of a solar tracker. Right: side view of a solar tracker.

the elasticity of the structure itself. They suggest that the right combination of stow positions, stiffness and damping policies can prevent the occurrence of this instability.

Suarez et al. developed a study using large-eddy simulations with the aim of explaining the mechanisms that govern the detachment of vortices (Suárez et al., 2022). A steady state sectional analysis of a solar tracker where the H/B ratio = 0.59; 0.67; 0.77 is presented; the angles of attack varying between −60° and +60°; and averaged and fluctuating load spectra are presented. From these spectra, the Strouhal number is determined for the different cases analysed. Additional significant studies regarding the wind effect on solar trackers in array conditions can be found in the work by Reina and De Stefano (2017) for a static case and in the work by Zhang et al. (2023b) for a sectional dynamic case.

Wind tunnel tests were also used to study the aeroelastic behaviour of a scale model of a complete tracker for different nominal angles of attack and two different torsional stiffness values (Martínez-García et al., 2021). They conclude that the observed phenomenon is a combination of torsional divergence and 1-degree-of-freedom flutter, which occurs when the angle of attack reaches a certain critical value (stall flutter). From the wind tunnel tests, they determined the stability curve of the tracker (critical wind speed vs. nominal angle of attack). They also studied how the angular moment of inertia and aspect ratio of the solar tracker affects the stability of the trackers (Martínez-García et al., 2021).

The current work has two objectives. First, to present a complete explanation of this instability from the point of view of fluid–structure interaction and how this interaction influences the dynamic response of PSTs. Second, to present a methodology, as general as possible, to determine the stability curve of any PST under two dimensional conditions, considering all the parameters that influence it (geometry, stiffness, inertia, nominal angle of attack, etc.).

To this end, a sectional model of the tracker with a torsional degree of freedom along its longitudinal axis (“torque tube”) is considered. The dynamics of the PST is studied considering both quasi-static loads and dynamic loads due to wind. The latter are formulated in terms of linear aerodynamic derivatives. To determine the aerodynamic derivatives, an extensive wind tunnel campaign is carried out for different ratios between the torque tube height and the PST chord.

In this work, linear aerodynamic derivatives are calculated, as is well known, independent of oscillation amplitude. For this reason, the theory of small perturbations is employed. As explained by Gao et al. (2023, 2018), even though linear derivatives do not consider amplitude dependence, they serve as an effective tool for critical point estimation. Detailed experimental procedures for obtaining linear aerodynamic derivatives, similar to those employed in this work, are exposed in studies conducted by Sarkar et al. (1994), Gu et al. (2001), and Ghowdhury and Sarkar (2003). Therefore, it should be noted that the procedure described in this work is valid for determining the critical velocity of the system but is not suitable for investigating post-flutter behaviour. To analyse what occurs after the critical velocity, one must use non-linear derivatives that depend on amplitude, as explained by Li et al. (2022). In this regard, the works of Noda et al. (2003) and Xu et al. (2016) experimentally investigate the amplitude dependence of these derivatives. Other significant studies on the nonlinearity of self-excited forces can be found in the works by Diana et al. (2013) and Náprstek et al. (2007), where nonlinear force models are proposed.

Fig. 3. Elements of an PST farm destroyed by wind-driven aeroelastic instability. Left: Oakey plant, Queensland, Australia (extracted from Gifford, 2019), right: Andalusia, Spain (extracted from Valentín et al., 2022).

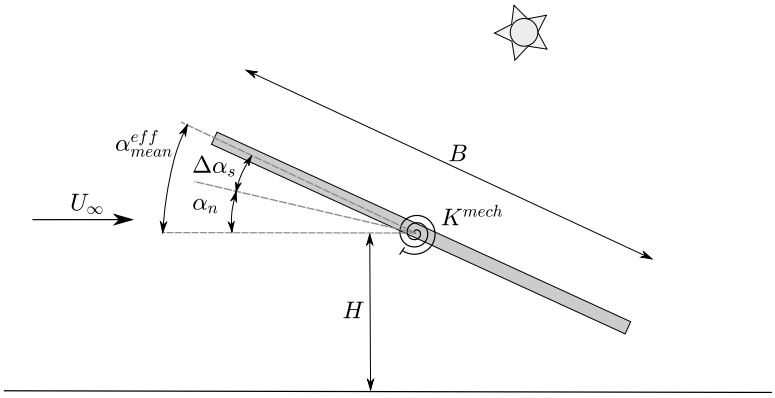

Fig. 4. Reference system. Notation explained in the list of symbols.

The test model and the methodology used are such that the values of the aerodynamic parameters (moment coefficient and aerodynamic derivatives) are obtained including the influence of both the inertial and elastic characteristics of the model itself. With this information, a general method is proposed to estimate the critical speed value by imposing the condition of zero effective damping. The results obtained with this procedure have been validated with tests in another wind tunnel on a specific case study. For the clearness sake and to limit the length of this article, the method presented in this work is restricted to the two-dimensional problem. The extension to the problem of a complete (three-dimensional) tracker can be easily done by using a modal decomposition of the dynamic response of the structure of a complete tracker.

The paper is organized as follows. The mathematical model used to study the stability of the trackers is presented in Section 2. The experimental setups used for the stability derivative determination and validation tests are described in Section 3. The results are summarized in Section 4, while Section 5 presents the validation method. Finally, some conclusions are drawn in Section 6.

2. Mathematical model

The mathematical formulation used is presented below. In Section 2.1 a description of the problem analysed and its formulation is given. In Section 2.2 the methods used to estimate the parameters of interest are described and, finally, in Section 2.3 an iterative method to determine the stability of the system under study is presented.

2.1. General formulation

Let us consider a two-dimensional flat solar tracker as shown in Fig. 4, with chord B, height of the rotation axis relative to the ground H, and nominal angle of attack α_n. The angle of attack is defined as the angle of the solar tracker to the horizon. The nominal angle of attack represents the theoretical angular position that the tracker should have as a function of the time of day to point at the Sun. If the solar tracker is immersed in a uniform wind of speed U_∞, it will undergo a static deflection, $\Delta\alpha_s$, which will modify its angle of attack. The static deflection, $\Delta\alpha_s$, can be estimated by establishing the equilibrium between the structural momentum and the aerodynamic momentum as

$$K^{mech}\Delta\alpha_s = \frac{1}{2}\rho U_\infty^2 B^2 C_m(\alpha_{mean}^{eff}, H/B), \tag{1}$$

K^{mech} being the structural stiffness per unit length ($[\mathrm{N\,m/m}]$), $1/2\rho U_\infty^2$ the dynamic pressure of the incident wind, C_m the coefficient of moment around the rotation axis, α_{mean}^{eff} the effective angle of attack of the solar tracker, $\alpha_{mean}^{eff} = \alpha_n + \Delta\alpha_s$ and H/B the ratio of the height of the solar tracker axis, H, to its chord, B. Note that the moment coefficient, C_m, is a function of both the effective mean angle of attack, and H/B ratio.

Therefore, the solar tracker with a given nominal angle, α_n, and subjected to an incident flow, U_∞, will have an effective mean angle of attack, α_{mean}^{eff}, different from the nominal angle of attack. Thus, for each wind condition and nominal angle, the static problem given by Eq. (1) must be solved to determine the effective mean angle of attack.

Once the static problem is solved and α_{mean}^{eff} estimated, the dynamic problem can be analysed considering a two-dimensional one-degree-of-freedom torsional problem, which can be modelled using the following constant coefficient ordinary differential equation:

$$J^{mech}\Delta\ddot{\alpha} + C^{mech}\Delta\dot{\alpha} + K^{mech}\Delta\alpha = M_{se}, \tag{2}$$

where J^{mech} represents the inertia ($[\mathrm{kg\,m^2/m}]$), and C^{mech} the structural damping ($[\mathrm{kg\,m^2/(s\,m)}]$). These structural characteristics are defined per unit length. $\Delta\alpha$ denotes the variation of the solar tracker angle of attack around its effective mean value, α_{mean}^{eff}. The right-hand term, M_{se}, represents the unsteady self-excited aerodynamic moment, which

can be expressed in the frequency plane as (Simiu and Scanlan, 1996; Scanlan and Tomko, 1971):

$$M_{se} = \frac{1}{2}\rho U_\infty^2 B^2 \left[kA_2^*(k, H/B, \alpha_{mean}^{eff})\frac{B}{U_\infty}\Delta\dot{\alpha} + k^2 A_3^*(k, H/B, \alpha_{mean}^{eff})\Delta\alpha \right] = -C^{aero}\Delta\dot{\alpha} - K^{aero}\Delta\alpha. \quad (3)$$

Thus, the aerodynamic moment is a function of the dynamic pressure of the incident wind, $1/2\rho U_\infty^2$; of the chord of the solar tracker, B; and the kinematic variables, $\Delta\alpha$, $\Delta\dot{\alpha}$, $\Delta\ddot{\alpha}$ and k. k is the reduced frequency, $k = \omega B/U_\infty$, and ω is the oscillation frequency of the motion. A_2^* and A_3^* are the dimensionless aerodynamic derivatives which are functions of the reduced frequency, k, the H/B ratio and the mean effective angle of attack, α_{mean}^{eff}. This formulation represents a linear model for the study of unsteady aerodynamic moments. There are other similar linear models that might be of interest to the interested reader (Zasso, 1996; Jensen, 1997).

The moment M_{se} is defined by two terms. One is proportional to the instantaneous angular position of the tracker, $\Delta\alpha$, and, therefore, is interpreted as an "aerodynamic stiffness" and the other term is proportional to the rotational velocity, $\Delta\dot{\alpha}$, and, therefore, is interpreted as an "aerodynamic damping". Calling K^{aero} and C^{aero} the aerodynamic stiffness and aerodynamic damping per unit length, respectively, Eq. (2) can be rewritten as:

$$J^{mech}\Delta\ddot{\alpha} + C^{mech}\Delta\dot{\alpha} + K^{mech}\Delta\alpha = -C^{aero}\Delta\dot{\alpha} - K^{aero}\Delta\alpha, \quad (4)$$

passing the aerodynamic contributions to the left-hand side, and defining an effective stiffness $K^{eff} = K^{mech} + K^{aero}$ and an effective damping $C^{eff} = C^{mech} + C^{aero}$, Gu et al. (2001), leads to

$$J^{mech}\Delta\ddot{\alpha} + C^{eff}\Delta\dot{\alpha} + K^{eff}\Delta\alpha = 0. \quad (5)$$

Taking into account Eqs. (3) and (5), the aerodynamic derivatives can be expressed as:

$$A_2^* = -\frac{2J^{mech}\left(\bar{C}^{eff} - \bar{C}^{mech}\right)}{\rho B^4 \omega}, \quad (6)$$

$$A_3^* = -\frac{2J^{mech}\left(\bar{K}^{eff} - \bar{K}^{mech}\right)}{\rho B^4 \omega^2}, \quad (7)$$

where $\bar{C}^{(\,)} = C^{(\,)}/J^{mech}$, and $\bar{K}^{(\,)} = K^{(\,)}/J^{mech}$. These expressions are analogous to those explained by Sarkar et al. (1994) and Chowdhury and Sarkar (2003). Since $\bar{C}^{eff} = 2\xi^{eff}\omega_n^{eff} = -2n^{eff}$, where ξ^{eff} is the effective damping coefficient, ω_n^{eff} the effective undamped natural frequency of the system, n the logarithmic decrement of the system response, and $\bar{K}^{eff} = \omega_n^{eff\,2}$, the expressions (6) and (7) can be rewritten as:

$$A_2^* = -\frac{2J^{mech}\left(-2\left(n^{eff} - n^{mech}\right)\right)}{\rho B^4 \omega}, \quad (8)$$

$$A_3^* = -\frac{2J^{mech}\left(\omega_n^{eff\,2} - \omega_n^{mech\,2}\right)}{\rho B^4 \omega^2}. \quad (9)$$

In this way, by measuring the mechanical logarithmic decrement, n^{mech}, (of the zero-wind system) and the effective logarithmic decrement, n^{eff}, for each wind speed, as well as the oscillation frequency of the system, ω, one can estimate the derivative A_2^* as a function of the reduced frequency $k = \omega U_\infty/B$. Likewise, by measuring the undamped mechanical natural frequency, ω_n^{mech}, (of the system without wind) and the effective undamped natural frequency, ω_n^{eff}, for each wind speed the derivative A_3^* can be estimated.

Therefore, to determine the aerodynamic derivatives A_2^* and A_3^* using (8) and (9) it is necessary to estimate the logarithmic decrement, n, and the oscillation frequency, ω.

For this purpose, an experiment has been designed (explained in Section 3.1) in which a model of a solar tracker with a certain angle of attack is taken out of its equilibrium position and released. By recording the rotational motion after release, both the logarithmic decrement, n, and the oscillation frequency, ω, are estimated with the methods detailed in Section 2.2. It should be noted that the zero-wind release tests, $U_\infty = 0$, allow us to determine the structural characteristics (n^{mech}, ω_n^{mech}) and the windy tests the effective characteristics (n^{eff}, ω_n^{eff}) as a function of velocity U_∞.

2.2. Logarithmic decrement, n, and frequency, ω, calculation

In this section, two different methods for estimating the logarithmic decrement, n, and frequency, ω, of a single degree-of-freedom torsional dynamic system are presented. The determination of n and ω is required, since, as shown in (8) and (9), they are necessary for the calculation of the aerodynamic derivatives.

Both methods are based on the torsional oscillation time signal collected after a release test (see Section 3.1). The first method, presented in 2.2.1, analyses the release signal in the time domain. The second method, presented in 2.2.2, analyses the release signal in the frequency domain by applying the discrete Fourier transform (DFT) with a fast Fourier transform algorithm (FFT).

2.2.1. Time domain

As can be deduced from the Eqs. (8) and (9) to determine of the derivative A_2^* (which is the one related to the damping of the system) it is required to determine the mechanical logarithmic decrement, n^{mech}, the effective logarithmic decrement, n^{eff}, and the oscillation frequency of the system, ω, and for the calculation of A_3^* it is necessary to determine the effective oscillation natural frequency, ω_n^{eff}, and the mechanical oscillation natural frequency, ω_n^{mech}.

To determine these parameters, tests were carried out on the solar tracker model descripted in Section 3.1. These tests consist of increasing the angle of attack of the model, taking it out of its equilibrium position, and then releasing it so that the system oscillates until it reaches a stationary condition. The oscillation of the model after release is registered by a laser distance measurement system. This release procedure is widely employed to ascertain the structural and effective characteristics of oscillatory systems, with notable works to be mentioned in this regard being (Chowdhury and Sarkar, 2005; Li et al., 2022; Sarkar et al., 2009; Andersen et al., 2016). This release procedure is performed systematically for different incident wind velocities, U_∞, and for different nominal angle conditions, α_n.

Once the post-release displacement of the model has been recorded, the logarithmic decrement of the signal, n, is calculated by exponential fitting to the measured displacement envelope. An example of a post-release displacement signal (blue line) and the exponential fit to estimate the logarithmic decrement (orange line) can be found in Fig. 5.

To check the measurement repeatability, a set of tests for case $H/B = 0.5$ were repeated twice. The repetitions were made for the whole speed range tested and for nominal angles between $\alpha_n \in [-30, 30]$. The relative error of the logarithmic decrements, n, between the pairs of repeated measurements was calculated and it was found that the mean error corresponds to 2% and the maximum error to 6.2%. These results indicate the tests are highly repeatable and therefore the calculated values of n are not influenced by the release.

The error between the release time series envelope and the fitted exponential was also analysed. The coefficient of determination, R^2, between the envelope and the fitted exponential was estimated for all cases performed in this work. The coefficient $R^2 = 1$ indicates a perfect fit between the envelope and the fitted exponential and $R^2 = 0$ indicates no similarity. The mean coefficient of determination for all the analysed cases was $R^2 = 0.98$, the maximum coefficient $R^2 = 0.99$ and the minimum $R^2 = 0.97$. These results indicate that the signal envelope fits well to an exponential shape and, therefore, the calculated logarithmic decrements are representative of the system behaviour. The estimated logarithmic decrement, n, according to this method is presented as a function of the reduced speed, U_r, in Fig. 8 (blue line). In this figure, error bars are added whose amplitudes represent the $1-R^2$ value, which

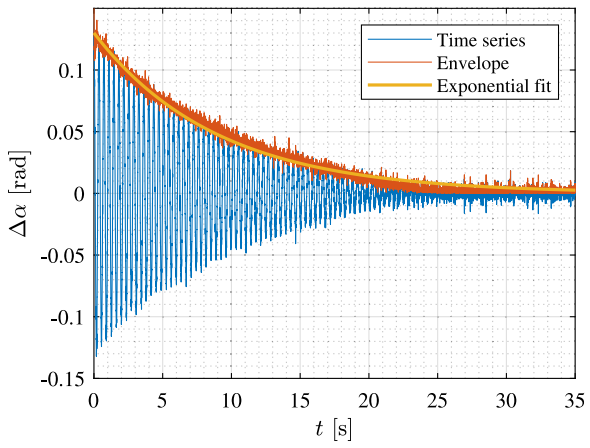

Fig. 5. Example of a post-release displacement signal. Variation of the angular position of the model, $\Delta\alpha$, as a function of time, t, (blue line), the envelope of the signal (red line) and the exponential fit to estimate the logarithmic decrement (orange line).

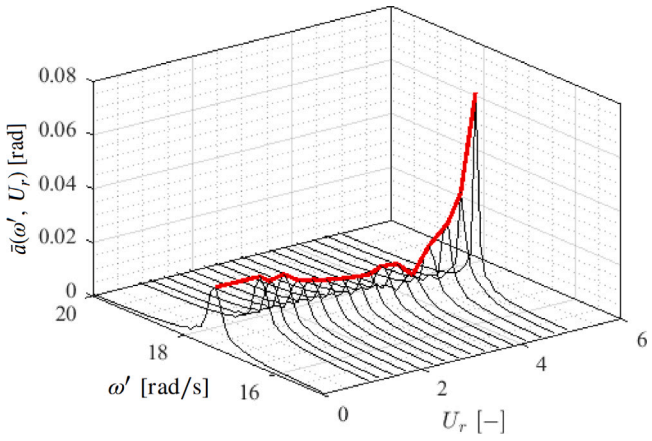

Fig. 6. Displacement spectra of the model, $\bar{a}(\omega', U_r)$, for different reduced incident wind speed, U_r, (for a nominal angle $\alpha_n = 10°$). Red line: spectra peak line.

remains approximately constant throughout the curve, indicating that the exponential nature of the release response is not greatly affected by the incident current velocity.

To estimate the system oscillation frequency after the release, ω, the signal is expressed in the frequency domain using the discrete Fourier transform and the dominant harmonic is determined. After estimating the logarithmic decrement, n, and the system oscillation frequency, ω, the damping coefficient, ξ, and the natural frequency, ω_n, can be calculated according to:

$$\omega_n^2 = \omega^2 + n^2; \quad \xi = -\frac{n}{\omega_n}. \tag{10}$$

As above mentioned, this release process is carried out for different incident wind speeds. The results obtained from the zero-wind release tests correspond to the purely mechanical parameters (n^{mech}, ξ^{mech} and ω_n^{mech}). And the results obtained from wind release tests correspond to the effective parameters, and will depend on the wind speed considered (n^{eff}, ξ^{eff} and ω_n^{eff}).

2.2.2. Frequency domain

Another procedure for system identification is to analyse the angular displacement time series in the frequency domain, computing the DFT of the displacement using a FFT algorithm, Duda et al. (2011). Referring to the work of Magalas and Malinowski (2003) is recommended if further exploration of the topic is sought. The displacement spectra of the model, $\bar{a}(\omega')$, for different reduced incident wind speed, defined as $U_r = (2\pi U_\infty)/(\omega_n^{mech} B) = U_\infty/(f_n^{mech} B)$, are shown in Fig. 6. In this figure, the maxima of the spectra, $\bar{a}(\omega'_{max})$, for each reduced speed, U_r, are marked in red. It should be noted that the surface shown in Fig. 6 is an example obtained for the case of $\alpha_n = 10°$, and each nominal angle of operation will have its own surface.

The plan view of the surface represented in Fig. 6 is shown in Fig. 7 left, where it can be noticed how the frequency of the dominant harmonic, ω'_{max}, varies as the reduced speed increases. From this plan view it is possible to estimate the frequency of the motion, ω, as a function of the reduced speed, U_r.

The side view of the surface in Fig. 6 is presented in Fig. 7 right. As can be noticed, the maximum value of the displacement spectrum, $\bar{a}(\omega'_{max})$, can be related to the reduced speed.

The aim of this procedure is to estimate the logarithmic decrement, n, by relating it to the maximum value of the displacement spectrum, $\bar{a}(\omega')$.

For this purpose, the acquired displacement signal of a test can be expressed as

$$\Delta\alpha(t) = \Delta\alpha_0 e^{nt} e^{i\omega t}. \tag{11}$$

An example displacement signal is shown in Fig. 5. The displacement is made up of three contributions: an initial value, which is the displacement applied to the model above its equilibrium position, $\Delta\alpha_0$; a sinusoidal component of frequency ω, $e^{i\omega t}$, which is expressed using a complex variable, $i = \sqrt{-1}$; and an exponential term containing the logarithmic decrement, e^{nt}.

Since the displacement measurements are discrete, expression (11) can be rewritten in the following form

$$\Delta\alpha_j = \Delta\alpha_0 e^{n\frac{t_m}{J}j} e^{i\omega\frac{t_m}{J}j}, \tag{12}$$

where t_m is the measurement time, J is the number of measurements, j is the time instant $j \in [0,\ J-1]$, and f is the frequency of the motion. Note that j becomes the variable indicating the instant of measurement and, therefore, $\Delta\alpha_j$ is identified with subscript j.

In general, if a discrete signal x_j is considered, the DFT of this signal, X_k, is calculated as

$$X_{\omega'} = \frac{1}{J}\sum_{j=0}^{J-1} x_j e^{-i\omega'\frac{t_m}{J}j}, \tag{13}$$

where ω' represents the frequency domain. Applying the expression (12) to Eq. (13) the spectrum is obtained

$$\bar{a}(\omega') = \frac{1}{J}\sum_{j=0}^{J-1} \Delta\alpha_0 e^{n\frac{t_m}{J}j} e^{i\omega\frac{t_m}{J}j} e^{-i\omega'\frac{t_m}{J}j}. \tag{14}$$

The maximum value of the spectrum amplitude, $\bar{a}(\omega')$, appears at $\omega' = \omega'_{max} = \omega$, and from (14) it is obtained

$$\bar{a}(\omega) = \frac{1}{J}\sum_{j=0}^{J-1} \Delta\alpha_0 e^{n\frac{t_m}{J}j}. \tag{15}$$

As can be seen from (15) the modulus of the harmonic $\bar{a}(\omega)$ corresponding to $\omega = \omega'$ coincides with the mean value of the exponential component. Finally, equating the modulus of the dominant harmonic $\bar{a}(\omega)$ to the mean of the exponential component of a continuous signal we reach at

$$\bar{a}(\omega'_{max}) \approx \frac{1}{t_m}\int_{t=0}^{t_m} \Delta\alpha_0 e^{nt} dt \approx -\frac{\Delta\alpha_0}{t_m n} \tag{16}$$

where the measurement time, t_m, has been considered to be sufficiently long to fulfil $a_0 e^{nt_m} \approx 0$.

The expression (16) allows to determine the logarithmic decay of the signal, n, as a function of the dominant harmonic of the Fourier transform.

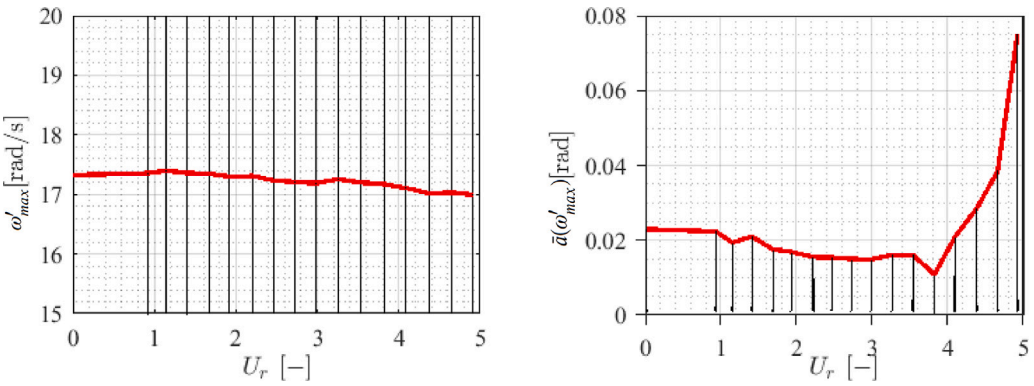

Fig. 7. Left: plan view of the surface represented in Fig. 6. Right: side view of the surface shown in Fig. 6.

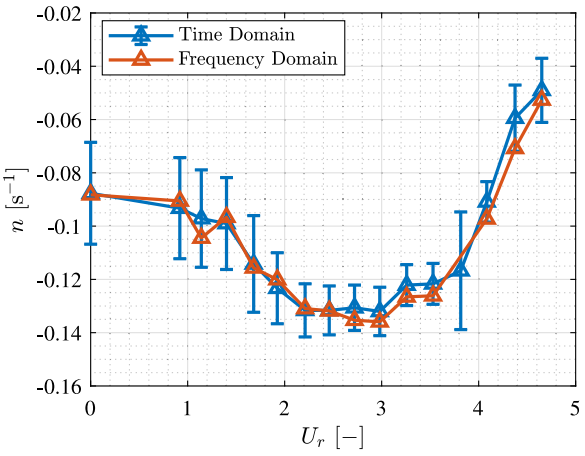

Fig. 8. Logarithmic decrement, n, as a function of the reduced speed, U_r, (for a nominal angle $\alpha_n = 10°$) estimated from the time domain (blue) including error bars indicating $1 - R^2$, and from the frequency domain (red).

In this way, it is possible to estimate, through the surface represented in Fig. 6, the characteristics of the system: ω and n as a function of U_r.

The logarithmic decrement, n, as a function of the reduced speed, U_r, for a nominal angle of $\alpha_n = 10°$, estimated from both the time domain and from the frequency domain, are compared in Fig. 8. In this figure, for the estimated logarithmic decrements according to the time domain, error bars have been included whose amplitudes indicate the value of $1 - R^2$, where R^2 is the coefficient of determination between the signal envelope and the fitted exponential functions, as explained in Section 2.2.1. As it is shown, both identification methods give quite close results.

2.3. Determination of the effective damping coefficient, ξ^{eff}, as a function of free stream velocity, U_∞, and nominal angle of attack, α_n

An iterative method to calculate the effective damping coefficient, ξ^{eff}, for a given wind speed, U_∞, specific geometrical conditions (B and H/B), and a nominal angle, α_n, is presented in this section. From the effective damping coefficient as a function of speed it is possible to analyse the dependence of the solar tracker damping with wind speed. This allows us to calculate at what speed the system is no longer damped and becomes unstable. The velocity at which $\xi^{eff} = 0$ is considered the critical speed, U_{crit}. Below this velocity $\xi^{eff} > 0$ and, therefore, an initial perturbation vanishes (stable system), however, above this velocity is $\xi^{eff} < 0$ and, consequently, the system will diverge (unstable system).

The Eqs. (8) and (9) can be rewritten as:

$$n^{eff} = \frac{\rho B^4 \omega}{4 J^{mech}} A_2^*(k, H/B) + n^{mech}, \text{ and} \tag{17}$$

$$(\omega_n^{eff})^2 = -\frac{\rho B^4 \omega^2}{2 J^{mech}} A_3^*(k, H/B) + (\omega_n^{mech})^2. \tag{18}$$

In addition, the damping coefficient and the oscillation frequency of an underdamped system follow the expressions

$$\xi^{eff} = -\frac{n^{eff}}{\omega_n^{eff}}, \text{ and} \tag{19}$$

$$\omega = \omega_n^{eff} \sqrt{1 - \xi^{eff}}, \tag{20}$$

respectively. Finally the reduced frequency is expressed as:

$$k = \frac{B\omega}{U_\infty}. \tag{21}$$

This set of 5 Eqs. (17)–(21) have 5 unknowns: ξ^{eff}, n^{eff}, ω_n^{eff}, ω and k. And they have the parameters: ρ and U_∞ (for the wind conditions); B, H, J^{mech}, n^{mech}, and ω_n^{mech} (for the mechanical and geometrical characteristics of the solar tracker); and the static coefficient of moment around the rotation axis, C_m.

To solve this system of equations and calculate the effective damping coefficient, the process shown in Fig. 9 is followed. Starting from an operating condition defined by the nominal angle, α_n, and the mechanical and geometrical characteristics of the solar tracker, the following procedure is followed:

- An incident wind speed is fixed U_∞.
- Using Eq. (1), the static deflection of the solar tracker is determined together with the effective mean angle, α_{mean}^{eff}.
- A tentative oscillation frequency of the system ω^* is chosen.
- With the wind speed fixed and the frequency chosen, the reduced frequency k is calculated using Eq. (21).
- With the reduced frequency, k, and the ratio H/B of the solar tracker, the values of the derivatives A_2^* and A_3^* are selected. It should be noted that for a given H/B and α_{mean}^{eff} one of the curves presented in this paper (in Sections 4.1 and 4.2) is chosen (for these figures, $\alpha_n = \alpha_{mean}^{eff}$, as the experimental setup described in Section 3.1 does not exhibit static deflection). If α_{mean}^{eff} does not coincide with any of the angles measured in this paper (which is to be expected) an interpolation is used.
- With the reduced frequency, k, the chosen oscillation frequency, ω^*, and A_2^* and A_3^*, using Eqs. (17) and (18), n^{eff} and ω_n^{eff} are calculated.
- Using n^{eff} and ω_n^{eff}, we calculate ξ^{eff} with Eq. (19).
- With ξ^{eff} and ω_n^{eff} the oscillation frequency of the system, ω is calculated using Eq. (20).
- If $\omega^* = \omega$, the estimated effective damping, ξ^{eff}, satisfies the system of equations for the fixed velocity U_∞. If $\omega \neq \omega^*$, another value of frequency ω^* is chosen, and the process is repeated.

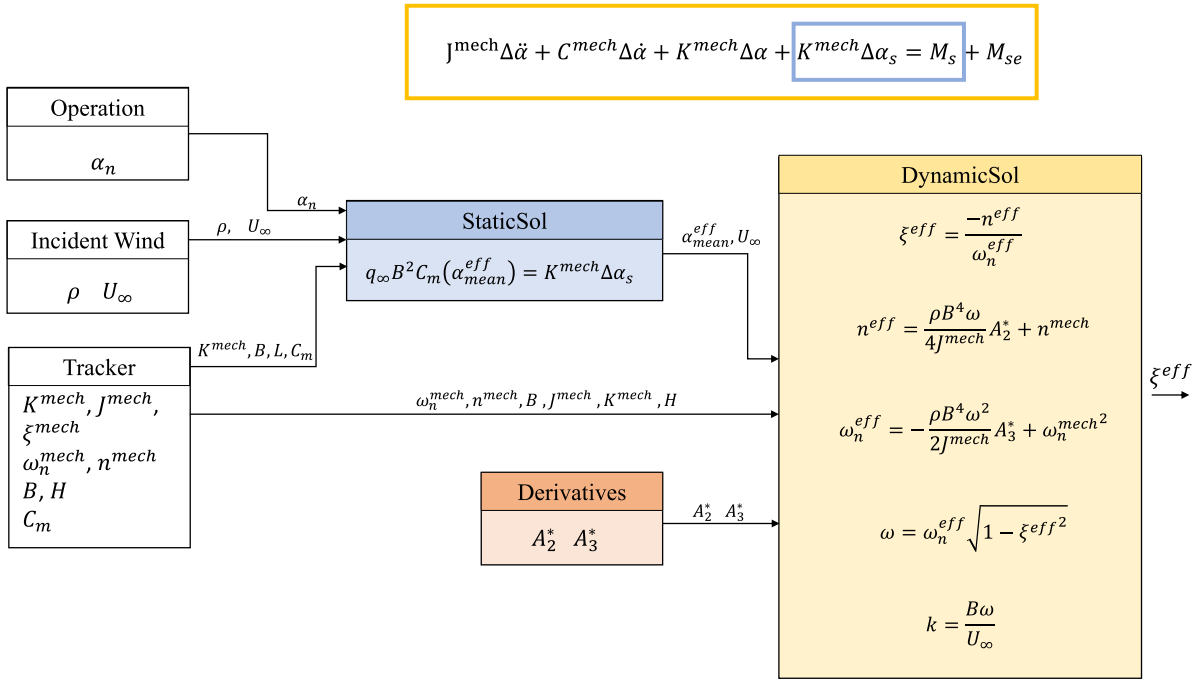

Fig. 9. Flow diagram of the effective damping coefficient, ξ^{eff}, calculation of a solar tracker from its operating conditions and geometry using the aerodynamic derivatives. StaticSol: equation to estimate the static deflection of the solar tracker, $\Delta\alpha_s$, and, therefore, the effective mean angle of attack α_{mean}^{eff}. DynamicSol: system of equations to solve the dynamics of the solar tracker. Derivatives: aerodynamic derivatives.

In this way the effective damping of the system can be estimated for each incident flow velocity. The velocity at which $\xi^{eff} = 0$ corresponds to the critical velocity.

An example of the effective damping coefficient, ξ^{eff}, estimated with the method described in this section, is shown in Section 5 (Fig. 22) as a function of reduced speed, U_r. This figure is discussed in detail in Section 5.

3. Experimental set-up

In this research, two different set-ups have been used, one for aerodynamic derivatives determination, and the other one for validation. Both set-ups are described in this section.

3.1. Experimental set-up for aerodynamic derivatives determination tests

Aerodynamic derivatives determination tests have been performed in the AB6 wind tunnel. The AB6 is an open circuit wind tunnel, with a 2.5 m × 0.5 m closed test section, 4 m length, with a 4.5:1 contraction ratio. A sketch of the wind tunnel is shown in Fig. 10. The flow at the test chamber is two-dimensional, with less than 1% differences along the vertical direction. The turbulence intensity is uniform and approximately than 3% for a flow speed of 25 m/s at the centre of the test section. Other turbulence intensities are not considered here, and therefore, further studies are required to investigate the effects of this parameter on the aerodynamic derivatives described in this work or on the critical velocities. In this regard, the study by Zhang et al. (2023a) can be referred to as it presented an investigation of the critical velocity of an isolated two-dimensional flat solar tracker for two different turbulence levels.

The model has been manufactured to reproduce the torsional motion of the solar tracker. To do that, a spring system has been located outside the wind tunnel (see Fig. 11). This system has been designed stiff enough so that the nominal angle of attack does not change with the static wind loads for increasing velocities. This means that there is no static deflection of the model, $\Delta\alpha_s \approx 0$, therefore $\alpha_{mean}^{eff} \approx \alpha_n$. It was verified that the maximum static deflection experienced by the model in this setup is consistently $\Delta\alpha_s < 0.2°$ for all conducted tests. The model has been placed in the centre of the wind tunnel, and a plate simulating the ground has been also placed. The value of H/B is changed by moving the plate up or down.

In this set-up, the aerodynamic derivatives are determined, as explained in Section 2.2.1. With these derivatives, the critical velocity values have been calculated. The tests consist in displacing the system from the equilibrium position and the leaving it to oscillate freely, recording the motion. The motion of the model has been measured with a laser displacement measuring system (Mikroelektronik M1L model). The sampling frequency of the instrument is 1000 Hz, and measurements have been taken for a sampling interval of 60 s. Simultaneously, the dynamic pressure of the flow has been recorded with a Pitot tube and a pressure capsule (Ashcroft CXLdp).

The solar tracker model placed inside the wind tunnel was manufactured with a flat plate of middle density fibre (MDF) with $B = 40$ cm, 0.5 cm thickness and length $L = 50$ cm, occupying the test section from wall to wall. The model is attached to the spring system outside the wind tunnel (Fig. 11) by means of a goniometer, of own manufacture, with one degree accuracy, which allows the angle of attack of the model to be modified. The model is supported by two bearings, one on each wall of the tunnel, so it has only one torsional degree of freedom. The structural characteristics of the model per unit length are: $K^{mech} = 84$ N m/(rad m), $\xi^{mech} = 0.01$, and $J^{mech} = 0.28$ kg m^2/m. The model inside the wind tunnel can be seen in Fig. 12. In that picture, the wind tunnel wall is not installed.

The choice of the model chord was determined as follows: firstly, considering that the reduced speed is defined as $U_r = U_\infty/(f.B)$, as discussed below, it is necessary to select a chord of sufficient size to ensure testing at low reduced speeds. Additionally, since the aerodynamic moment is proportional to $1/2\rho U_\infty^2 B^2$ (see Eq. (3)), a chord of sufficient size must be chosen to ensure that the aerodynamic moment is significant enough to appreciably modify the effective characteristics of the system during release tests. On the other hand, the model chord should not be excessively large to avoid interference with blockage. For these reasons, the selected chord size was determined.

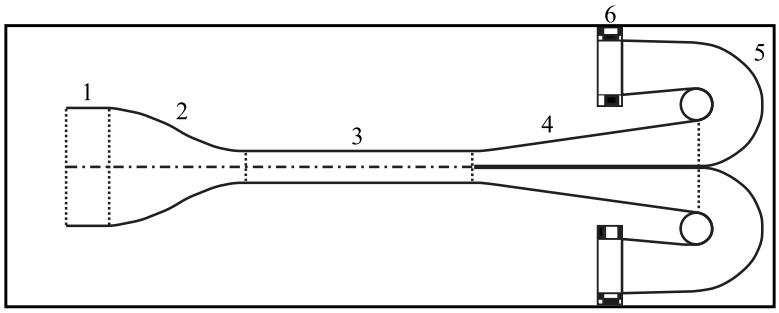

Fig. 10. Sketch of the AB6 wind tunnel: (1) grid; (2) contraction; (3) test section; (4) diffuser; (5) flow turning semicircular diffuser; (6) fans.

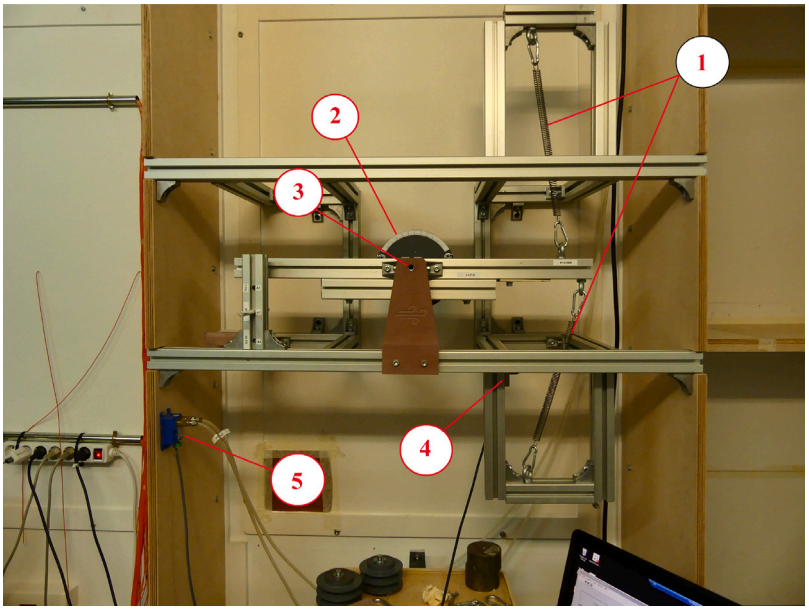

Fig. 11. View of the setup for providing torsional stiffness to the solar tracker in the main set-up. The structure is placed outside the wind tunnel, attached to one of the walls. Labels: (1) compression springs; (2) goniometer; (3) rotation axis; (4) laser; (5) pressure capsule.

Fig. 12. View of the model inside the wind tunnel.

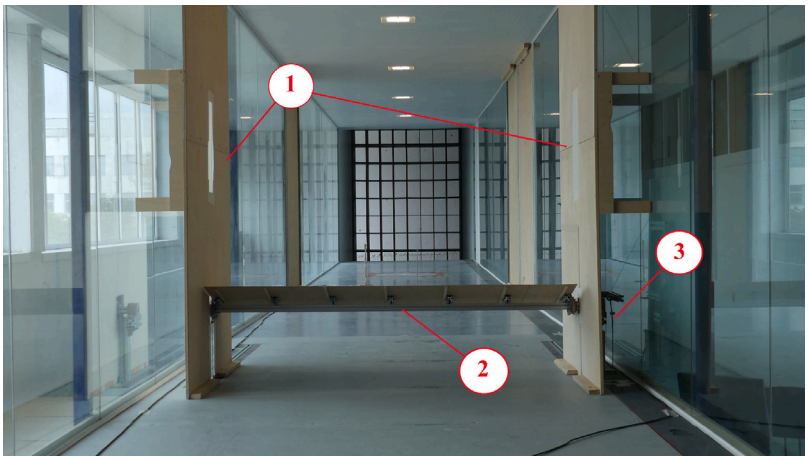

Fig. 13. View of the solar tracker in the auxiliary set-up. The picture is taken inside the tunnel towards the air inlet direction. Labels: (1) endplates (2) solar tracker model (3) system to displace the model from its equilibrium position.

The tests have been repeated for several values of the height-to-width parameter H/B (see Fig. 4). The values that have been tested are $H/B = 0.3,\ 0.4,\ 0.5,\ 0.6,\ 1$, and 2. For each of the height-to-width values, the nominal angle of attack (marked as α_n in Fig. 4) has been varied. The angles tested are $\alpha_n = 0°, \pm5°, \pm10°, \pm20°, \pm30°, \pm40°$. For the lower heights, some of the angles could not be tested because of the proximity to the floor. Specifically, $\alpha_n = \pm30°$ and $\alpha_n = \pm40°$ were excluded for $H/B = 0.3$, and $\alpha_n = \pm40°$ for $H/B = 0.4$. This leads to a maximum blockage ratio of 10%.

The tests were limited to angles within the range of ±40° because, for lower H/B ratios ($H/B = 0.3$ and 0.4), the model could not be tested at higher absolute nominal angles as it would collide with the ground. However, it is considered that the tested range is of significant interest since it corresponds to cases with the lowest reduced critical velocities based on the literature consulted. An example of this is in the study by Zhang et al. (2023a), where the so-called unstable and sub-stable zone is found within the range of ±30°.

3.2. Experimental set-up for validation

One of the characteristics of the main experimental setup for aerodynamic derivatives determination is that the stiffness of the model is sufficiently high so that there is no static deflection, $\Delta\alpha_s = 0$, and therefore the curves of A_2^* and A_3^* can be presented for constant angles of attack. This implies that to calculate the effective damping coefficient, ξ^{eff}, for a particular tracker at a given incident free stream velocity, U_∞, and nominal angle of attack, α_n, it is necessary to first estimate the static deflection of the tracker, $\Delta\alpha_s$, using Eq. (1), and then use A_2^* and A_3^* derivatives corresponding to the effective mean angle of attack of the case under study, $\alpha_{mean}^{eff} = \alpha_n + \Delta\alpha_s$ (see Section 2.3).

To validate this procedure, an auxiliary experimental set-up was arranged. It consists of a solar tracker with structural characteristics $K^{mech} = 20$ N m/(rad m), $J^{mech} = 0.1$ kg m^2/m, and $\xi^{mech} = 0.03$, and geometrical characteristics $B = 0.62$ m, and $L = 1.7$ m. This solar tracker presents static deflection as a function of the incident wind speed. The idea is to test this model for a specific case of $H/B \approx 0.5$ and different nominal angles of attack and to calculate the critical speed obtained.

At the same time, the process presented in Section 2.3 is used to calculate the critical velocities of a solar tracker with the same structural characteristics as the model of the secondary experimental setup. Using the aerodynamic derivatives obtained with the main experimental setup.

The results obtained from both procedures are compared in Section 5. This comparison serves as validation of the aerodynamic derivatives presented in this work.

Table 1
Structural characteristics of the solar tracker under study per unit length.

Parameter	Main experimental setup	Secondary experimental setup	Units
J^{mech}	0.28	0.10	kg m^2/m
K^{mech}	84	20	N m/(rad m)
ξ^{mech}	0.01	0.03	[–]

The auxiliary tests have been performed in the ACLA16 wind tunnel. It is an open circuit wind tunnel, with a 2.2 m × 2.2 m closed test section, 17 m length, with a 2:1 contraction ratio. The turbulence intensity is less than 2% for a flow speed of 20 m/s at the location of the solar tracker axis. A detailed description of this wind tunnel can be found in Lopez-Nuñez et al. (2020).

In this case, the model also reproduces the torsional motion of the solar tracker with a spring system. The spring system is placed inside the wind tunnel, but endplates have been provided so that the aerodynamics characteristics of the solar tracker are not affected. The tracker is placed near the ground of the wind tunnel. A view of the wind tunnel with the model installed and the endplates is shown in Fig. 13.

Again, the solar tracker is turned outside the equilibrium position and left to vibrate in the incoming wind. The motion is again measured with a laser displacement measuring system (Mikroelektronik M1L model), but the sampling time has been reduced to 30 s, keeping the sampling frequency constant at 1000 Hz. Simultaneously, the flow dynamic pressure has been measured by using a Pitot tube and a pressure capsule (Ashcroft CXLdp).

The critical speed has been estimated, in the auxiliary set-up, as the velocity at which, once the solar tracker is released, it does not return to the equilibrium position and keeps oscillating ($\xi^{eff} = 0$).

For a better comparison, the structural values of the elastic properties of both setups are displayed in Table 1.

4. Results

In this section the aerodynamic derivatives A_2^* and A_3^*, obtained using the set-up described in Section 3.1 and procedure described in Section 2.1, are presented, as a function of reduced speed, $U_r = U_\infty/(f.B)$, for different H/B conditions and different nominal angles, α_n. Because this experimental setup has enough torsional stiffness to ensure the model does not exhibit static deflection over the range of speeds tested, the nominal angles, α_n, at which the derivatives are presented coincide with the effective angles, α_{mean}^{eff}, around which the model oscillates. This allows the stiffness of the model to be decoupled from the aerodynamic derivatives obtained. If the model had static

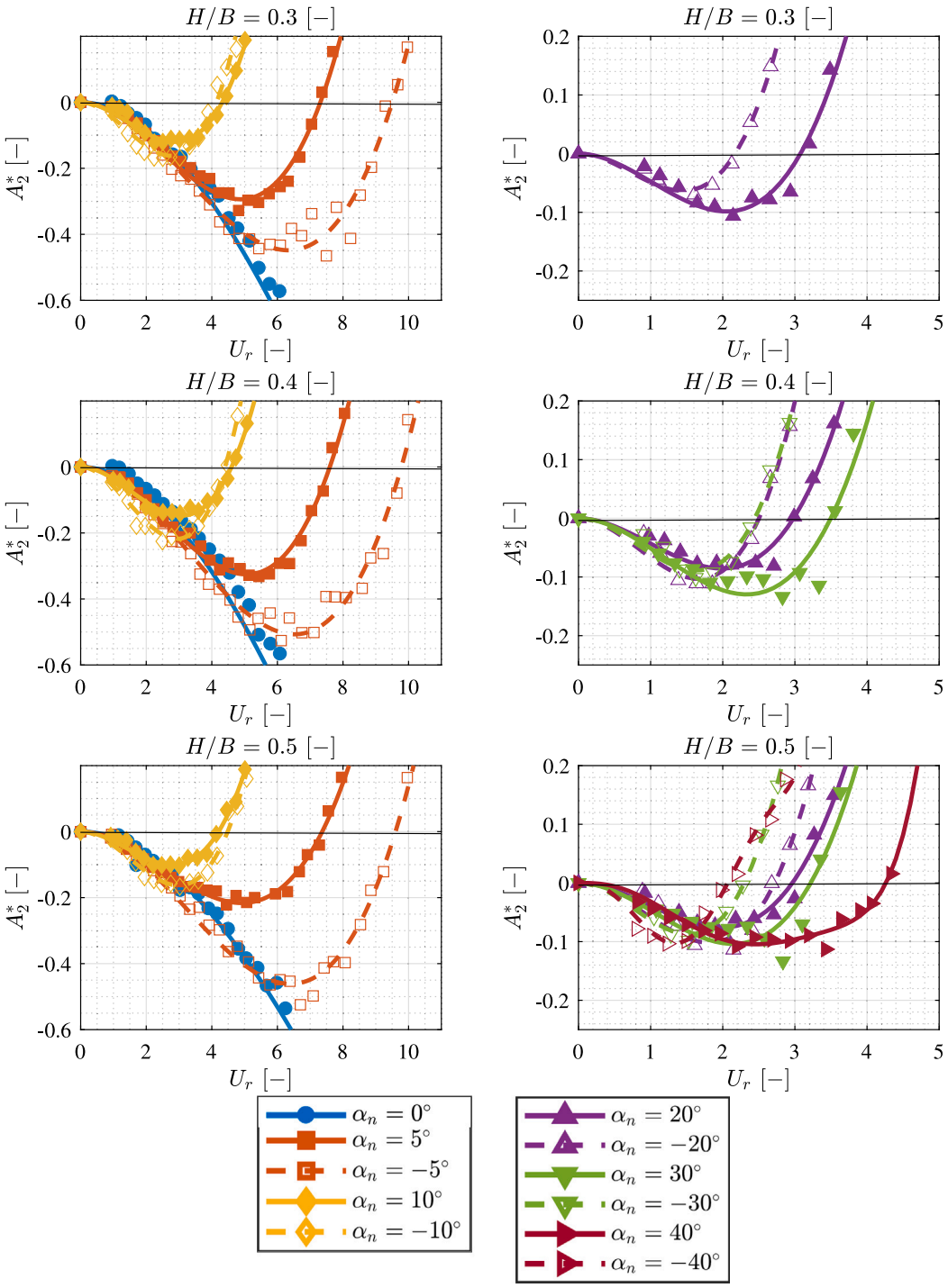

Fig. 14. Aerodynamic derivative A_2^* as a function of the reduced wind speed, U_r, for different tracker chord-height ratios ($H/B = 0.3$, 0.4 and 0.5), and different nominal angles of attack, α_n. Symbols: experimental data. Lines: polynomial fitting curves (solid line: positive angle, dashed line: negative angle).

deflection, the effective angle around which the model oscillates would have to be estimated for each condition of incident wind speed. It has been decided to present the A_2^* and A_3^* derivatives as a function of the reduced speed U_r instead of the reduced frequency, k, since the authors consider that this facilitates the interpretation of the results, as well as being a usual form of representation, Taylor and Browne (2020).

4.1. Sensitivity analysis of aerodynamic derivative A_2^* to H/B

The aerodynamic derivative A_2^* as a function of the reduced wind speed, $U_r = U_\infty/(f.B)$, for different tracker chord-height ratios, H/B, and different nominal angles of attack, α_n, is presented in Fig. 14 (H/B = 0.3, 0.4 and 0.5) and Fig. 15 (H/B = 0.6, 1.0 and 2.0). The plots on the left show cases of nominal angles of attack with small absolute values ($|\alpha_n|$ = 0°, 5°, 10°). The plots on the right show cases of nominal angles with large absolute value ($|\alpha_n|$ = 20°, 30°, 40°). The symbols indicate experimental data. The lines are third degree polynomials: $A^*_{2,fit} = A_p + B_pU_r + C_pU_r^2 + D_pU_r^3$ fitted to the experimental data. Since $A_2^* = 0$ when $U_r = 0$ imposes that $A_p = 0$. A second condition, $dA_2^*/dU_r = 0$ when $U_r = 0$, is also imposed, which implies that $B_p = 0$. This second condition has been imposed as it allows for a better fit to the experimental data at low reduced

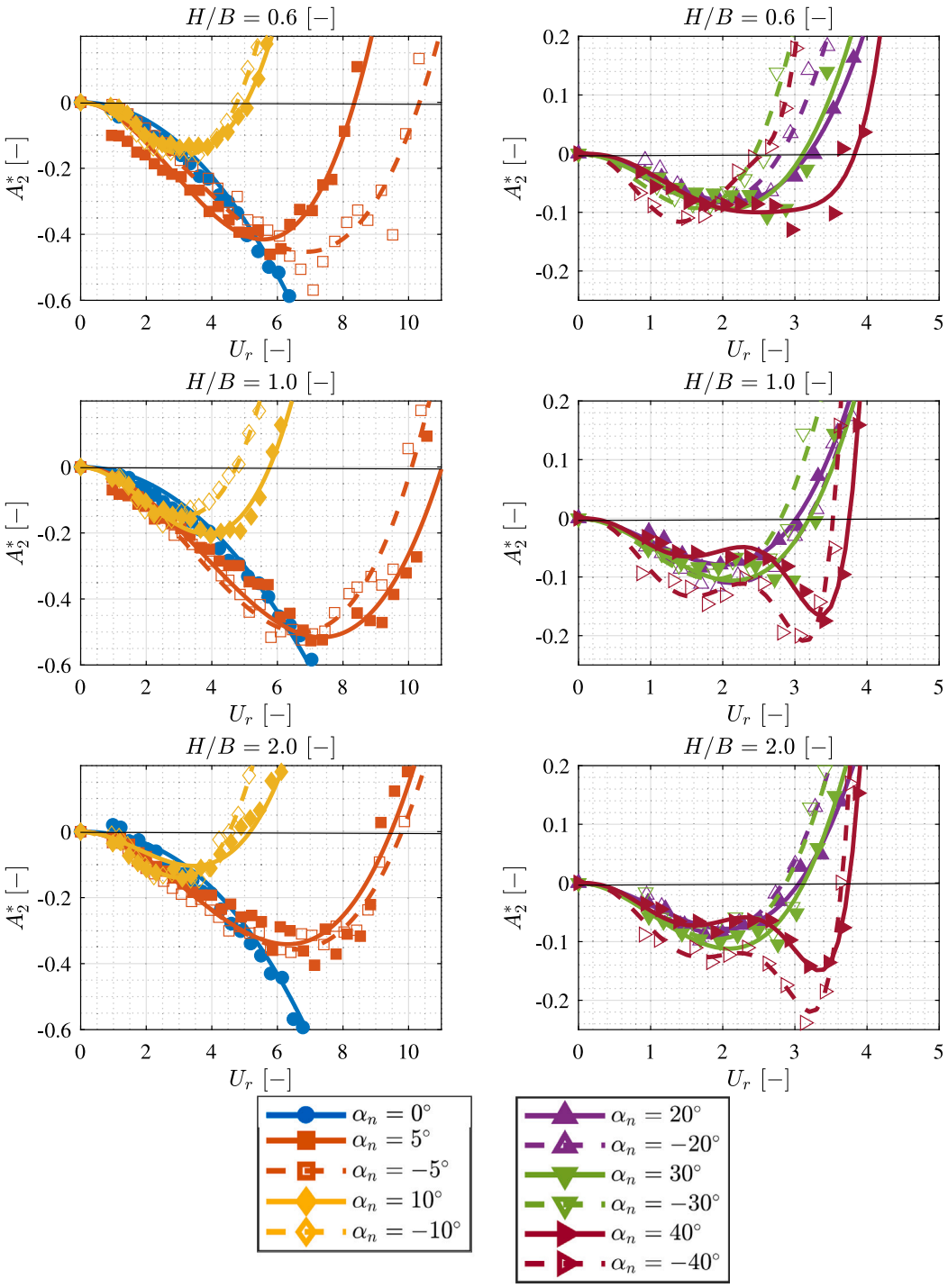

Fig. 15. Aerodynamic derivative A_2^* as a function of the reduced wind speed, U_r, for different tracker chord-height ratios ($H/B = 0.6$, 1.0 and 2.0), and different nominal angles of attack, α_n. Symbols: experimental data. Lines: polynomial fitting curves (solid line: positive angle, dashed line: negative angle).

speeds ($U_r < 2$). For the ±40° case, the third-degree polynomial fit proved inadequate, requiring an increase in polynomial order, resulting in $A^*_{2,fit,40} = D_pU_r^3+E_pU_r^4+F_pU_r^7$. The mean coefficient of determination for all the fittings applied to the experimental data of the aerodynamic derivatives in this study was $R^2 = 0.91$, with a standard deviation of $\sigma_{R^2} = 0.08$.

Note that the results have been divided between small nominal angles of attack ($\alpha_n = 0°$, $|\alpha_n| = 5°$ and $|\alpha_n| = 10°$) and large nominal angles of attack ($|\alpha_n| = 20°$, $|\alpha_n| = 30°$ and $|\alpha_n| = 40°$). The reason for this distinction is that large angles of attack are noticeably more unstable than small ones and, therefore different scales in U_r are used in Figs. 14 and 15 for small angles (left plots) and for large angles (right plots).

For $|\alpha_n| = 40°$ (Figs. 14 and 15) no measurements were taken at $H/B = 0.3$ or $H/B = 0.4$ to avoid damaging the model due to the proximity to the ground. The same happens for $|\alpha_n| = 30°$ at $H/B = 0.3$

The curves of the derivative A_2^* as a function of the reduced speed for the different nominal angles have similar shapes. As shown, for a reduced speed of $U_r = 0$ (no wind conditions) the derivative $A_2^* = 0$, this implies, as expected, at this U_r condition there is no aerodynamic damping. As the reduced speed increases, the derivative A_2^* decreases. This suggests that, as the speed increases, the aerodynamic damping,

C^{aero}, increases and, consequently, the system is more stable since it will present a higher effective damping, $C^{eff} = C^{mech} + C^{aero}$.

As shown, for the different nominal angles, there is a reduced speed at which the derivative A_2^* reaches its minimum value. This point will be called $P1$. From $P1$ ahead the behaviour of A_2^* changes and as the wind speed increases the aerodynamic derivative increases and again reaches zero. The point where the derivative reaches zero again is called point $P2$. Therefore, between $U_r = 0$ and $P2$ the aerodynamic actions result in an increase of the effective damping since $A_2^* < 0$. The maximum effective damping is at $P1$. For reduced wind speed values above $P2$ the derivative A_2^* is positive and increasing. Consequently, from $P2$ ahead the effect of aerodynamics is unfavourable as the effective damping of the system is reduced. It can become unstable when $C^{eff} = 0$. For that reason, the point $P2$ gives us a measure of how stable a solar tracker will be from an aerodynamic point of view. Larger values of $P2$ indicate a larger range of reduced wind speed in which the aerodynamics are favourable.

It should be noted that for the case $\alpha_n = 0°$ the A_2^* curve is always decreasing with reduced speed, U_r. Accordingly, the points $P1$ and $P2$ do not appear in this case. This behaviour agrees with Theodorsen solution for small amplitudes in which an torsional oscillating flat plate never reaches positive values of A_2^* and, as a consequence, would not present instabilities (Theodorsen, 1949). According to Strømmen (2010) and Scanlan and Tomko (1971), the aerodynamic derivatives A_2^* and A_3^* can be theoretically expressed using Theodorsen's complex circulation function, $C(k) = F(k) + iG(k)$, as

$$A_{2,theo}^* = -\frac{\pi}{8k}\left(1 - F(k) - 4G(k)\frac{1}{k}\right) \tag{22}$$

and,

$$A_{3,theo}^* = \frac{\pi k}{2}\left(\frac{F(k)}{k} - \frac{G(k)}{4}\right), \tag{23}$$

where the subscripts "theo" refer to Theodorsen's formulation. Aerodynamic derivatives obtained experimentally for a case of $\alpha_n = 0°$ and $H/B = 2$ are compared with those calculated using Eqs. (22) and (23) as a function of the reduced speed, U_r, in Fig. 17. Additionally, derivative A_3^* is compared to the quasi-steady solution, as explained in Strømmen (2010) and Taylor and Browne (2020), which takes the form

$$A_{3,qst}^* = \frac{C_{m,\alpha}}{k^2}, \tag{24}$$

being $C_{m,\alpha}$ the slope of the static coefficient of moment curve with $\Delta\alpha$. The experimental case of $\alpha_n = 0°$ and $H/B = 2$ was selected due to its high comparability with Theodorsen's solution which corresponds to the potential solution of a flat plate oscillating around zero angle of attack without ground effect. It is worth noting that the experimental solution exhibits the same trend as the theoretical results, with A_2^* monotonically decreasing, as discussed previously, and A_3^* monotonically increasing. Furthermore, it can be observed that the experimental solution maintains a strong agreement with Theodorsen's solution until approximately $U_r = 6$, after that the theoretical solution underestimates the absolute values of both A_2^* and A_3^*. This discrepancy may be attributed either to the ground effect or to the fact that the theoretical solution corresponds to a potential case and, therefore, does not account for viscosity effects.

However, solar trackers exhibit instabilities for nominal angles $\alpha_n = 0°$, even though A_2^* is never positive. This is because, although the nominal angle without wind is $\alpha_n = 0°$, as the speed of the incident wind increases, the mean effective angle of the solar tracker, α_{mean}^{eff}, will change, due to the low torsional stiffness of these systems.

Therefore, as the wind speed increases, the mean effective angle, α_{mean}^{eff}, of the solar tracker changes and is no longer zero, which can lead to instabilities. Therefore, the authors recommend that the aerodynamic derivatives be obtained with models of high torsional stiffness, as is the case presented in this study, to avoid or reduce the influence of the angle change with wind speed. In this way, the derivatives obtained will only depend on the aerodynamic conditions and not on the stiffness of the model tested. An example of the application of these derivatives, obtained with a model of high torsional stiffness, for the estimation of critical speeds, will be shown in Section 5.

In addition, A_2^* for the case of $\alpha_n = 0°$ and different H/B ratios is also presented in Fig. 16, for a larger range of U_r.

4.1.1. Aspect ratio H/B influence on $P1$ and $P2$

The influence of aspect ratio H/B on the points $P1$ (minimum value of A_2^*, $A_{2,min}^*$) and $P2$ (reduced speed at which $A_2^* = 0$, $U_r\ |_{A_2^*=0}$), is shown in Figs. 18 and 19 respectively.

For simplicity, the cases of nominal angles with low absolute value ($|\alpha_n| = 5°$ and $|\alpha_n| = 10°$) are shown in an one plot, and the cases of nominal angles with high absolute value ($|\alpha_n| = 20°$, $|\alpha_n| = 30°$ and $|\alpha_n| = 40°$) on other plot. In one hand, as mentioned above, for the cases of $\alpha_n = -10°$ and $\alpha_n = -5°$ the value of U_r at $P2$ does not vary significantly with H/B. On the other hand, for the cases of $\alpha_n = 5°$ and $\alpha_n = 10°$, a maximum value is reached in both cases when $H/B = 1.0$. Therefore, at the ratio $H/B = 1.0$ these nominal angles present their most stable behaviour. Additionally, in the cases of nominal angles with large absolute values, as H/B increases, U_r at $P2$ of the positive configuration decreases while U_r at $P2$ of the negative configuration increases until both cases match for $H/B = 2.0$. The largest differences in U_r at $P2$ values between the positive and negative angles appear at $H/B < 1$.

Point $P1$, the minimum A_2^* value, $A_{2,min}^*$, as a function of H/B and the nominal angle of the solar tracker, α_n, is shown in Fig. 19.

Once again, for a clear presentation, the plots for small absolute nominal angles and large nominal angles have been separated. For $\alpha_n = 5°$ and $\alpha_n = 10°$, the lowest $A_{2,min}^*$ is obtained for $H/B = 1.0$. As can be noticed from expression (6) this implies that the maximum effective damping, C^{eff}, for these angles is obtained at $H/B = 1.0$. Another remarkable aspect is the value of $A_{2,min}^*$ reached at $H/B = 0.5$ for $\alpha_n = 5°$ and $\alpha_n = 10°$, which does not seem to follow the expected trend. The reason of this behaviour cannot be concluded from the experimental data obtained in this study. Future work with flow visualization, for example, would be required to attempt an explanation for why the minimum value of A_2^* is so high for $H/B = 0.5$ at $\alpha_n = 5°$ and $\alpha_n = 10°$. Besides, for the large nominal angles, the minimum value of A_2^* is not quite affected with H/B, except for $\alpha_n = -40°$, which decreases drastically from $H/B = 0.6$, showing a clear difference with $\alpha_n = 40°$.

In both Figs. 19 and 18, as well as in Figs. 14 and 15, it can be observed that the most significant differences between the derivative A_2^* for angles of opposite sign but the same absolute value occur in the cases of $\alpha_n = \pm 40°$. This may be attributed to as the absolute value of the angle of attack increases, in the presence of the ground, the geometric configuration difference between positive and negative angles becomes more pronounced. For instance, at $\alpha_n = 40°$, the cross-sectional area for airflow passage defined between the ground and the solar tracker decreases as one progresses in the wind direction. Conversely, at $\alpha_n = -40°$, this cross-sectional area increases as one advances in the wind direction. This disparity in configuration between positive and negative angles diminishes as the absolute value of the angle of attack decreases or the H/B ratio is increased.

4.2. Sensitivity analysis of aerodynamic derivative A_3^* to H/B

The aerodynamic derivative A_3^* as a function of the reduced wind speed, U_r, for different tracker chord-height ratios, H/B, and different nominal angles of attack, α_n, is presented in Fig. 20 ($H/B = 0.3$, 0.4 and 0.5) and Fig. 21 ($H/B = 0.6$, 1.0 and 2.0). The plots on the left show cases of nominal angles of attack with small absolute value ($|\alpha_n| = 0°$, 5°, 10°), and on the right the nominal angles with large absolute value ($|\alpha_n| = 20°$, 30°, 40°). The symbols indicate experimental data. The lines

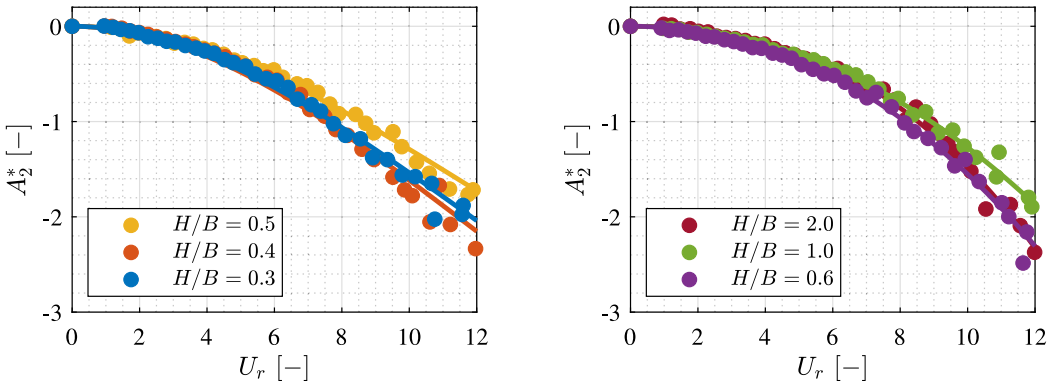

Fig. 16. Variation of aerodynamic derivative A_2^* as a function of reduce speed, U_r, for a nominal angle $\alpha_n = 0$, and different aspect ratios H/B.

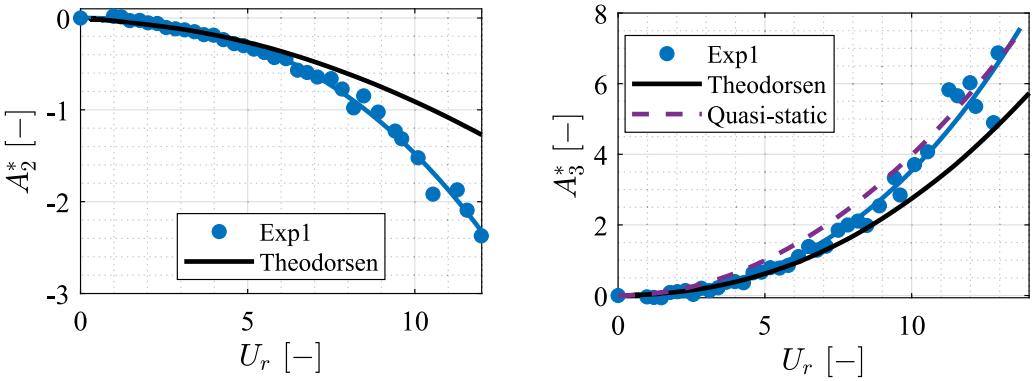

Fig. 17. Aerodynamic derivatives A_2^* and A_3^* obtained experimentally for a case of $\alpha_n = 0°$ and $H/B = 2.0$ compared to Theodorsen's solution (solid black line) and the quasi-static solution (dashed purple line), as a functions of the reduced speed, U_r.

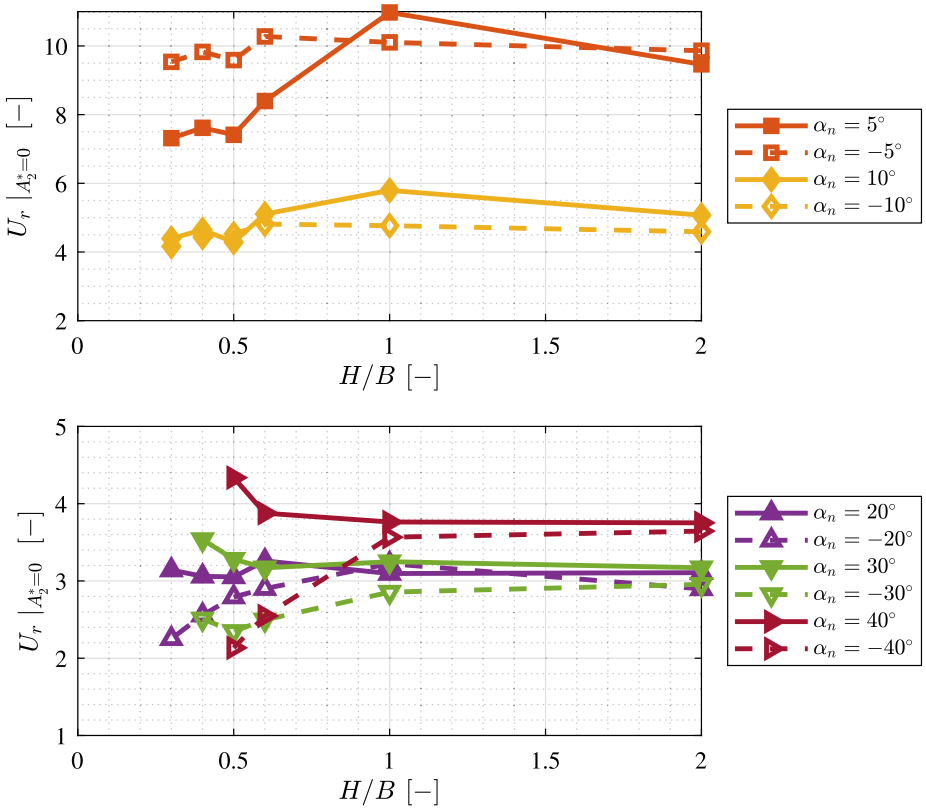

Fig. 18. Critical speed at which $A_2^* = 0$, $U_r\,|_{A_2^*=0}$, as a function of the aspect ratio H/B, for several values of the nominal angle of the solar tracker, α_n.

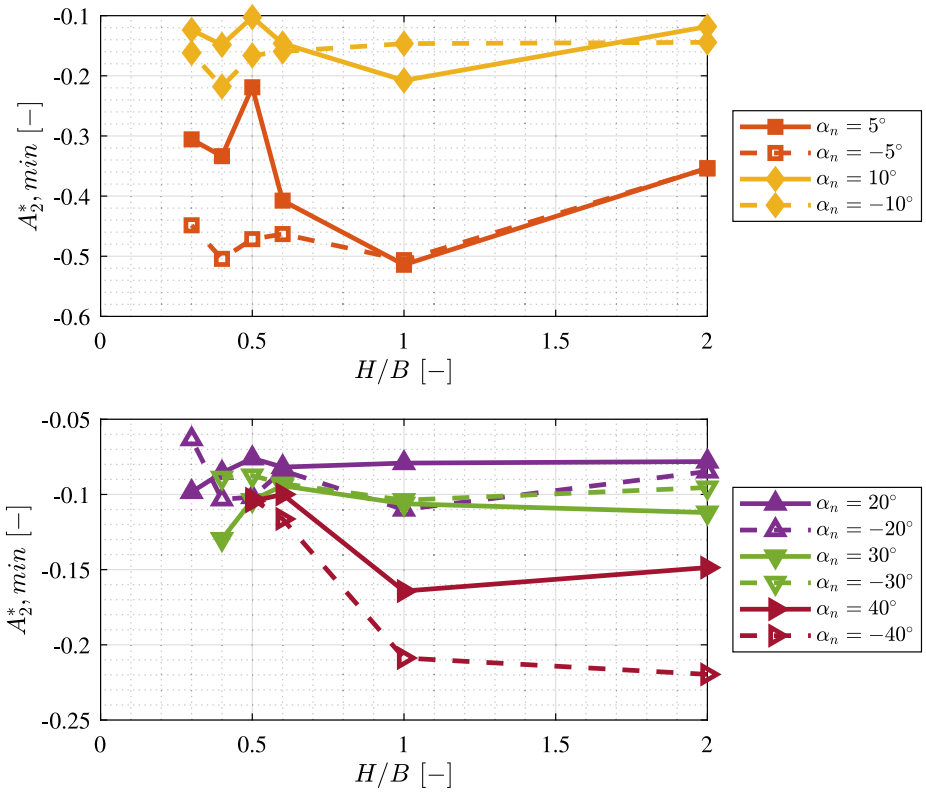

Fig. 19. Minimum value of aerodynamic derivative A_2^* as a function of aspect ratio H/B, for several values of the nominal angle of the solar tracker, α_n.

are a third degree polynomial: $A^*_{3,fit} = A_p + B_p U_r + C_p U_r^2 + D_p U_r^3$ fitted to experimental data. Since $A_3^* = 0$ when $U_r = 0$ imposes that $A_p = 0$. A second condition, $\mathrm{d}A_3^*/\mathrm{d}U_r = 0$ when $U_r = 0$, is also imposed which implies that $B_p = 0$. This second condition has been imposed as it allows for a better fit to the experimental data at low reduced speeds ($U_r < 2$).

A_3^* is shown in Figs. 20 and 21, as a function of U_r for different nominal angles, α_n, and different H/B ratios. All curves monotonically increase, showing the same tendency, which implies according to (7) that the effective stiffness, K^{eff}, of the solar tracker decreases as the reduced speed, U_r, increases. This behaviour has already been described by Taylor and Browne (2020). As A_3^* remains always positive, no U_r condition in which the effective stiffness increases has been found, according Eq. (7). This is the reason why the analysis of this derivative is less complex than A_2^*, where there were favourable and unfavourable conditions from the aerodynamic point of view, as described in 4.1.

For nominal angles of small absolute value ($|\alpha_n| = 0°$, $|\alpha_n| = 5°$ and $|\alpha_n| = 10°$) it is found that A_3^* does not vary markedly with H/B. For nominal angles of large absolute value ($|\alpha_n| = 20°$, $|\alpha_n| = 30°$ and $|\alpha_n| = 40°$) it is shown that negative angles have higher A_3^* than positive nominal angles. A clear example can be noticed for $\alpha_n = 20°$ and $\alpha_n = -20°$ at $H/B = 0.3$. This implies that in large nominal angles the decrease of effective stiffness, K^{eff}, as U_r increases, is greater in negatives than positives angles. Additionally, as it is shown for $\alpha_n = 40°$ and $H/B > 0.5$, derivative $A_3^* \approx 0$ for the different values of U_r tested. Thus, there is no change in the effective stiffness of the system as the reduced speed increases.

In addition, the difference in the slope of derivative A_3^* between small and large angles of attack is to be emphasized. As can be observed in Figs. 20 and 21, the slope of A_3^* for angles of $|\alpha_n| = 30°$ and $|\alpha_n| = 40°$ is notably different from smaller angles of attack. This behaviour may be related to that for angles greater than $\alpha_n = 10°$ or less than $\alpha_n = -10°$, the two-dimensional solar tracker is in a stall under static conditions, as evidenced in Fig. 24, which presents the coefficient of moment on the tracker axis as a function of the effective mean angle of attack. Although the phenomenon is dynamic, it is expected that if the tracker is oscillating around an angle at which it would stall under static conditions, the flow may detach during parts of the oscillation cycle. In contrast, for smaller angles where the flow would be attached under static conditions, it could be expected that there is less flow detachment during the oscillation cycle than in the case of large angles. Based on the results, one could assume that oscillating around an angle beyond the static stall implies that aerodynamic effects have a smaller influence on the variation in effective stiffness, as indicated by the smaller slopes in the A3 curve for these cases. However, these hypotheses cannot be corroborated with the experimental measurements presented in this study, as they are displacement measurements, and there are no, for example, velocity field measurements around the tracker during the oscillation cycles. Therefore, complementary studies would be necessary to conclude how flow detachment affects the variation in effective stiffness.

5. Case study and validation of results

In this section, the reduced critical speed, $U_{r,crit}$, of a solar tracker is calculated in two different ways. This is intended as a validation of the procedure introduced in Section 2.3. The first method is using the validation set-up, as described in Section 3.2 and the second method using the aerodynamic derivatives presented in Section 2 and the process described in Section 2.3. The characteristics of the solar tracker under study are: $B = 0.62$ m, $L = 1.7$ m, $H/B = 0.5$, $K^{mech} = 20$ N m, $J^{mech} = 0.1$ kg m^2, and $\xi^{mech} = 0.03$.

Following the procedure described in Section 2.3, the reduced critical speeds, $U_{r,crit}$, of the solar tracker under study have been calculated. The procedure requires as input data, as explained in Section 2.3, the mechanical characteristics of the solar tracker under analysis (K^{mech}, J^{mech} and ξ^{mech}) in addition to the geometrical characteristics (H, B and L). With the structural and geometrical data together with the aerodynamic derivatives corresponding to the H/B ratio under study,

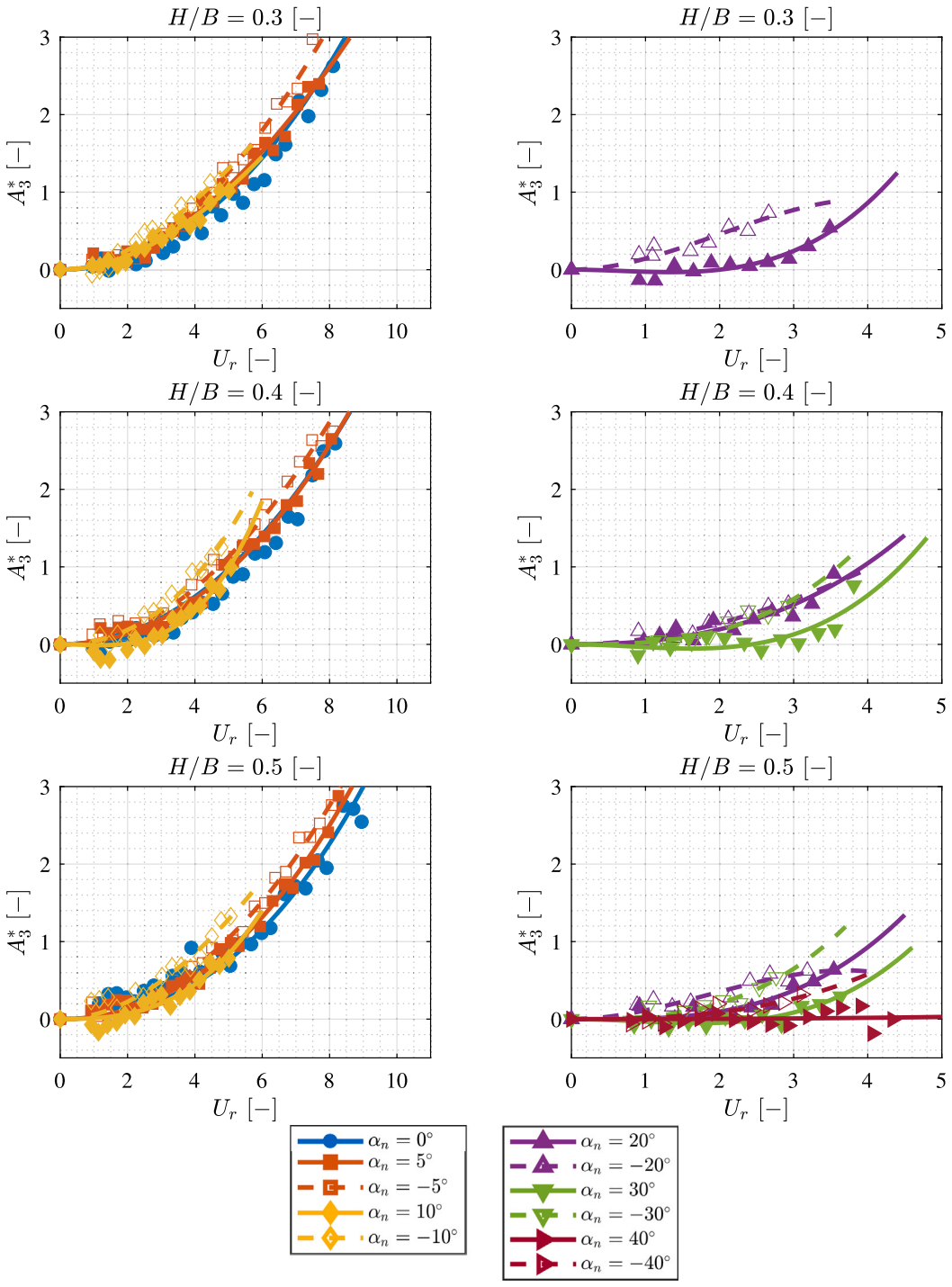

Fig. 20. Aerodynamic derivative A_3^* as a function of the reduced wind speed, U_r, for different tracker chord-height ratios ($H/B = 0.3$, 0.4 and 0.5), and different nominal angles of attack, α_n. Symbols: experimental data. Lines: polynomial fitting curves (solid line: positive angle, dashed line: negative angle).

the critical speed for the different nominal angles of the solar tracker, α_n, is estimated.

The determination process of critical reduced speed for condition $\alpha_n = 10°$ is detailed below as an example. For different reduced speeds studied, the static deflection of the solar tracker, $\Delta\alpha_s$, was first calculated, using Eq. (1), and the effective mean angle of attack, α_{mean}^{eff}, is obtained. The effective mean angle minus the nominal angle of attack of the solar tracker under study is shown in Fig. 22 (top left) as a function of reduced speed, U_r. It is shown that the tracker for low reduced speeds has little static deflection and the effective mean angle remains close to 10°. However, as the reduced speed increases, the change in the mean effective angle is noticeable, reaching $\alpha_{mean}^{eff} = 14°$ for $U_r = 3.5$. For each of these reduced speeds and effective mean angles, using the procedure described in Section 2.3, the effective damping coefficient, ξ^{eff}, shown in Fig. 22 (top right) is obtained as a function of the reduced speed. As can be noticed, for $U_r = 0$ the effective and structural damping coefficient coincide, $\xi^{eff} = \xi^{mech}$, as there is no aerodynamic influence. As the reduced speed increases, the effective damping coefficient increases until it reaches a maximum value, in this case close to $\xi^{eff} = 0.06$ for $U_r = 2.5$. From this speed onwards, the trend changes drastically and the effective damping coefficient decreases rapidly, reaching $\xi^{eff} = 0$ for a value close to

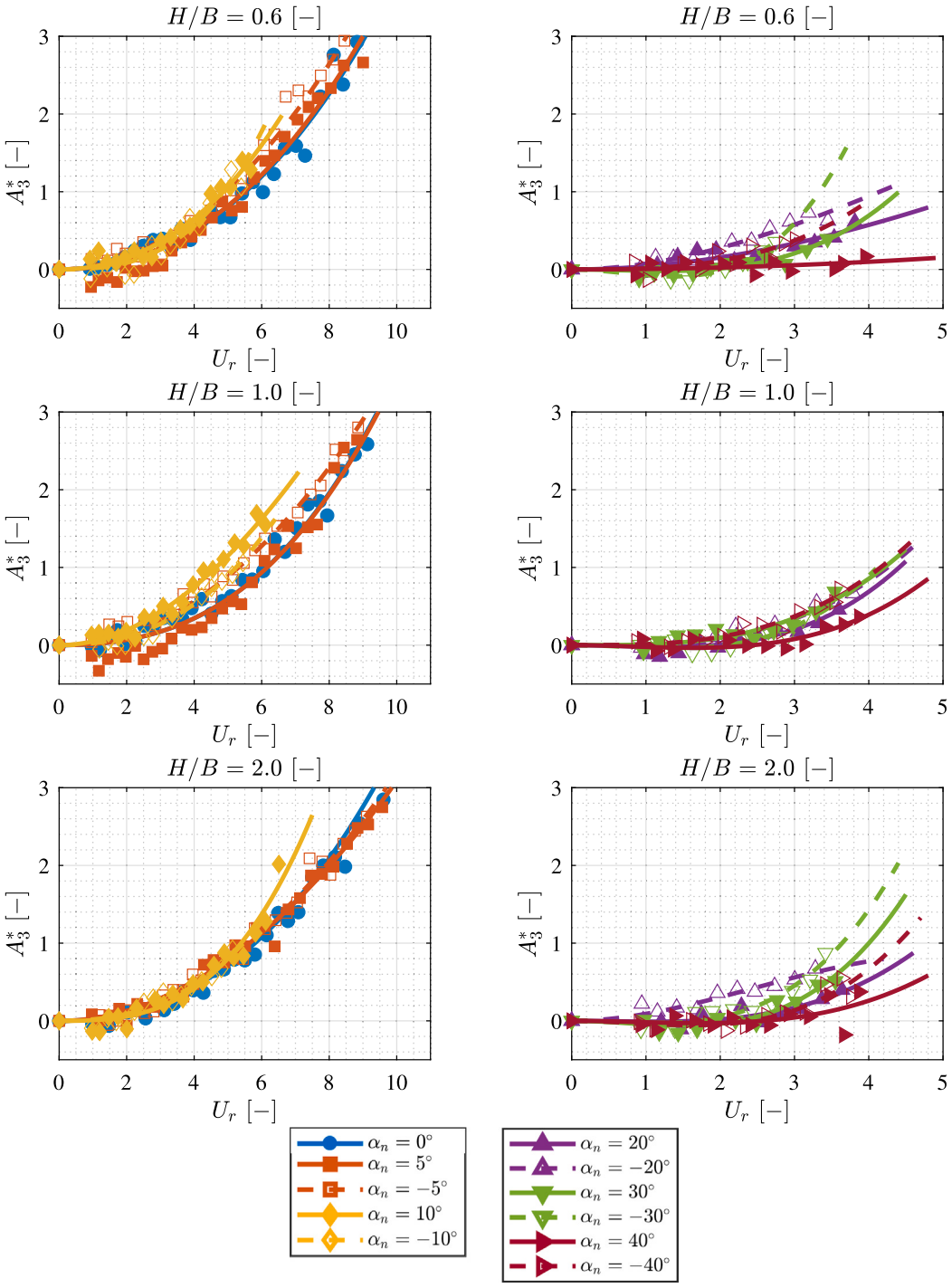

Fig. 21. Aerodynamic derivative A_3^* as a function of the reduced wind speed, U_r, for different tracker chord-height ratios ($H/B = 0.6$, 1.0 and 2.0), and different nominal angles of attack, α_n. Symbols: experimental data. Lines: polynomial fitting curves (solid line: positive angle, dashed line: negative angle).

$U_r = 3.2$, which corresponds to the reduced critical speed, $U_{r,crit}$, since for higher reduced speeds $\xi^{eff} < 0$ and therefore the system would diverge.

To validate the results and the calculation procedure, test in a auxiliary experimental setup (presented in Section 3.2) have been carried out with the solar tracker under study in the ACLA16 aerodynamic tunnel.

The stability curve of the tracker under study is shown in Fig. 23. The stability curve relates the reduced critical speed, $U_{r,crit}$, to the nominal angle of the solar tracker, α_n. Therefore, for reduced speeds higher than the critical speed the system will be unstable and for reduced speeds lower than the critical speed the system will be stable. It should be noted again that the nominal angle of operation of the solar tracker, α_n, does not correspond to the effective mean angle of the tracker, α_{mean}^{eff}, since there is a static deflection, $\Delta\alpha_s$, due to the incident wind speed. This static deflection can be estimated by using Eq. (1). To calculate the static deflection, it is necessary to know the moment coefficient, C_m, as a function of the effective mean angle (Fig. 24). This coefficient has been determined by measuring the static deflection of the solar tracker, $\Delta\alpha_s$, of the auxiliary set-up and the dynamic pressure,

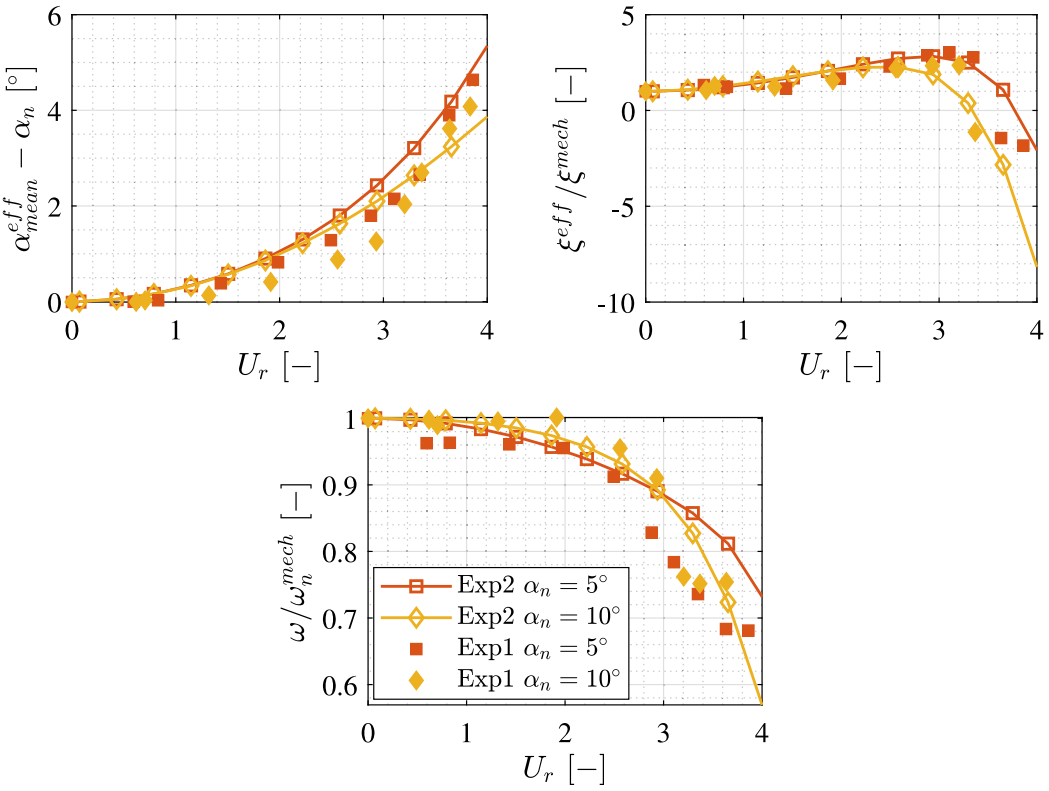

Fig. 22. Top left: Effective mean angle of attack minus nominal angle, $\alpha^{eff}_{mean} - \alpha_n$, as a function of reduced speed, U_r. Top right: Effective damping coefficient divided by the structural damping coefficient, ξ^{eff}/ξ^{mech}, as a function of U_r. Bottom: Oscillation frequency divided by the natural structural oscillation frequency, ω/ω^{mech}, as a function of U_r. For $\alpha_n = 5°$ and $\alpha_n = 10°$, $H/B = 0.5$. Predicted using the procedure of Section 2.3 (Exp2), and experimental of validation set-up (Exp1).

$1/2\rho U^2_\infty$, according to

$$C_m(\alpha^{eff}_{mean}) = \frac{K^{mech}\Delta\alpha_s}{1/2\rho U^2_\infty B^2}. \tag{25}$$

The influence of the aspect ratio $H/B = 0.5$ on the static coefficient is noticeable, the moment coefficient differs quite a bit from being asymmetric between positive and negative effective mean angles. The static moment coefficients obtained by Zhang et al. (2023a) at $H/B = 2.05$ and by Taylor and Browne (2020) are also presented in Fig. 24.

As shown in Fig. 23, the results obtained with the model described in Section 2.3 exhibit a good agreement with the results obtained in the validation tests performed in the auxiliary experimental setup for the case of large angles of attack. Conversely, for small angles of attack, it can be noted that the value of the maximum critical reduced speed has been accurately determined, but both results do not align regarding the angle of attack at which it is achieved. This discrepancy may be attributed to, as discussed in Section 4.1, low angles of attack are highly reliant on static deflection to reach critical conditions (as observed in the case of $\alpha_n = 0°$, where the absence of static deflection would eliminate the instability). Consequently, uncertainties in estimating the effective mean angle, which may arise from solving Eq. (1) or uncertainties in angular positioning, could impact the estimated critical velocities. However, since large angles of attack are inherently more unstable, as discussed in Section 4.1, the influence of static deflection is not as significant, and therefore, uncertainties in its estimation do not substantially affect the results.

It should be noted that the aerodynamic derivatives were calculated with a different experimental setup with different mechanical characteristics per unit length (K^{mech}, J^{mech} and ξ^{mech}) and different geometrical characteristics (B, L, H), except for the H/B ratio. This proves that the aerodynamic derivatives obtained with a model whose mechanical stiffness is adequately high to avoid static deflection only depend on the H/B ratio and, in addition, it validates the aerodynamic derivatives presented in this work.

To further study the validity of the model described in Section 2.3, the corresponding data for $\alpha = 5°$ are also displayed in Fig. 22, allowing for a comparison between the effective damping, ξ^{eff}, effective mean angle of attack, α^{eff}_{mean}, and predicted oscillation frequency, ω, with the experimental measurements of the validation set-up. As observed in the figure, the model presented in Section 2.3 predicts the trends observed in the experimental results. In particular, the good agreement of the data concerning effective damping is noteworthy. Concerning the effective mean angle of attack, once again, it can be noted how the model predicts the trend; however, it overestimates the static deflection of the tracker by approximately 1° for reduced speeds $2 < U_r < 3$ and $\alpha_n = 10°$. This could be attributed to $\alpha_n = 10°$ is close to the point of static stall entry for the tracker (see Fig. 24), and therefore, the resolution of Eq. (1) may introduce more uncertainty due to the nonlinearity of the aerodynamic static moment. Finally, regarding the oscillation frequency, it is evident that the model predicts the experimental results for low reduced speeds, but as the system approaches unstable conditions, the predictions become overestimated. Nevertheless, it should be emphasized that this study has been conducted with the aim of examining an isolated two-dimensional case (without trackers in front or behind), which corresponds to the cases more commonly presented in the literature, for example the works conducted by Zhang et al. (2023a) and Taylor and Browne (2020). Therefore, the method described does not consider three-dimensional effects and could not be used to investigate self-excited phenomena in a three-dimensional tracker.

6. Conclusions

General conclusions are listed below:

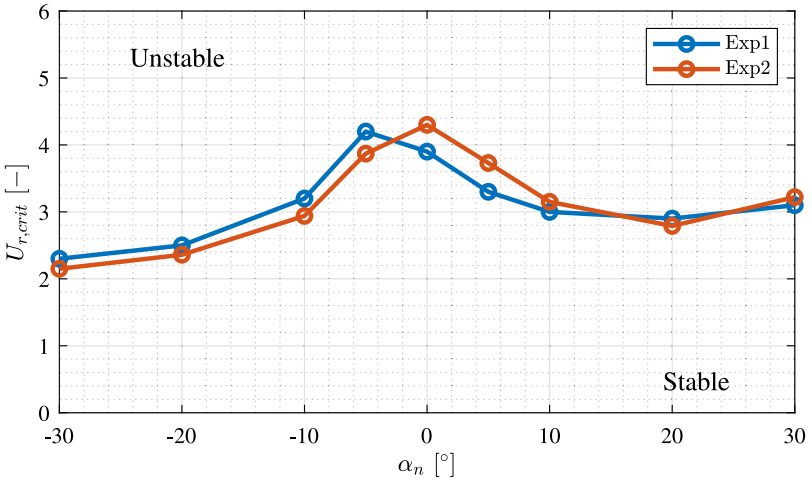

Fig. 23. Stability curve of the solar tracker under study. Exp1: validation testing set-up. Exp2: procedure described in Section 2.3 using aerodynamic derivatives.

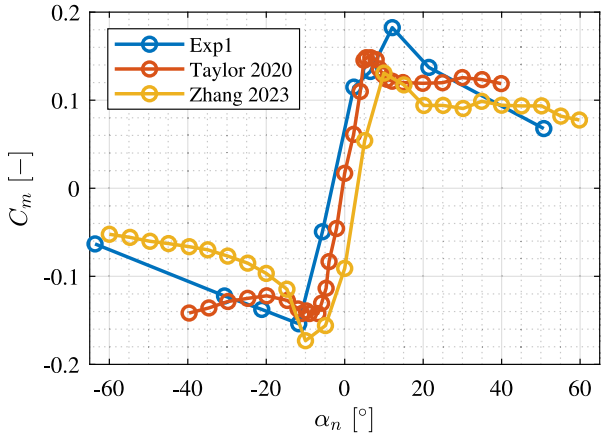

Fig. 24. Moment coefficient, C_m, as a function of the effective mean angle, α^{eff}_{mean}. Exp1: experimental set-up for validation, H/B = 0.5. Zhang 2023: data from Zhang et al. (2023a) at $H/B = 2.05$. Taylor 2020: data from Taylor and Browne (2020).

- Aerodynamic derivatives, A^*_2 and A^*_3, for a basic solar tracker model have been experimentally obtained for a wide range of nominal angles of attack ($\alpha_n \in [-40°,\ 40°]$) and 6 different H/B aspect ratios. These data can be used to estimate the critical speed of this type of solar tracker in a wide range of configurations by applying the method described in Section 2.3 to determine the effective damping, ξ^{eff}, as a function of incident wind speed, U_∞.
- The validity of the method for estimating the effective damping coefficient was tested by comparing results obtained with two different experimental set-ups. The use of a model with high torsional stiffness in the main experimental setup allows the aerodynamic derivatives presented in this work to depend only on the model geometry (H/B and nominal angle of attack, α_n) and the wind speed, U_∞. Therefore, they can be used to study the stability of a two-dimensional solar tracker for any structural characteristics (J^{mech}, C^{mech} and K^{mech}).
- It should be noted that linear aerodynamic derivatives have been employed, wherein the influence of oscillation amplitude is not taken into account. As a result, this method allows for the estimation of the critical velocity but is not suitable for the investigation of post-flutter behaviour. To study the behaviour beyond the critical velocity, it would be necessary to use non-linear aerodynamic derivatives (dependent on amplitude), Noda et al. (2003), Li et al. (2022), Xu et al. (2016) and Gao et al. (2023).
- In addition, it should also be noted that this method is applicable for isolated two-dimensional cases and, in principle, could not be employed to investigate the self-excited behaviour of solar trackers under three-dimensional conditions.

Conclusions regarding derivative A^*_2 are listed below:

- A^*_2 is significantly influenced by H/B. To analyse this influence, the point $P2$ (reduced speed, U_r, at which $A^*_2 = 0$) has been defined. As from $U_r = 0$ to $P2$ the derivative $A^*_2 < 0$ and therefore the aerodynamic damping is positive (see Eq. (6)), the point $P2$ gives us a guess about how stable the configuration at a given nominal angle is, since it indicates the critical speed range in which the aerodynamic damping favours stability.
- It was found that cases $\alpha_n = 5°$ and $\alpha_n = 10°$ have a maximum value of U_r at $P2$ when aspect ratio $H/B = 1$ (see Fig. 18 top). Therefore, $H/B = 1$ is the condition that maximizes the stability of these angles.
- For large $|\alpha_n|$ ($|\alpha_n| = 20°,\ 30°$ and $40°$) and $H/B < 1$ the positive angles have higher U_r at $P2$ than their negative counterparts. As H/B increases this difference decreases until for $H/B = 2$ the positive and negative angles with the same absolute value have the same U_r at $P2$ (see Fig. 18 bottom).
- At $\alpha_n = 0$, A^*_2 is monotonically decreasing (see Fig. 16), so $P2$ cannot be defined and, therefore, this angle is always stable. However, as has been commented throughout the paper, as the incident wind speed, U_∞, increases, the solar tracker changes its angle of attack, due to static reflection, $\Delta\alpha_s$, and, therefore, the effective mean angle, α^{eff}_{mean}, does not coincide with the nominal angle (defined at $U_\infty = 0$). This explains why a solar tracker at $\alpha_n = 0$ presents instability, because as U_∞ increases, the effective mean angle changes, reaching angles of attack that present instability.
- Related to the previous point, it is essential, in order to analyse the stability, to take into account the static deflection, $\Delta\alpha_s$, of the tracker and to determine the effective mean angle, α^{eff}_{mean}.

Conclusions regarding derivative A^*_3 are listed below:

- A^*_3 monotonically increases as reduced speed increases, and it has no change of sign. This is found for all angles and aspect ratio H/B tested. Since A^*_3 always has a positive sign, the effective stiffness always decreases as the incident flow speed increases.
- A^*_3 is not very sensitive to the H/B ratio. Furthermore, it has been found that large negative nominal angles ($\alpha_n = -40°$, $\alpha_n = -30°$ and $\alpha_n = -20°$) have higher A^*_3 values than positive ones

(α_n = 40°, α_n = 30° and α_n = 20°). This implies that operating conditions with large negative nominal angles reduce effective stiffness, K^{eff}, as U_r increases to a greater extent than positive angles.

CRediT authorship contribution statement

Juan A. Cárdenas-Rondón: Investigation, Formal analysis, Writing – original draft. **Mikel Ogueta-Gutiérrez:** Data curation, Conceptualization, Writing – original draft. **Sebastián Franchini:** Resources, Supervision, Writing – original draft. **Raul Manzanares-Bercial:** Visualization.

Declaration of competing interest

The authors declare that they have no known competing financial interests or personal relationships that could have appeared to influence the work reported in this paper.

Data availability

Data will be made available on request.

Acknowledgements

The authors would like to thank Javier Pascual Alonso, Carlos Pascual Alonso, Manuel Ortega Hidalgo, Guillermo Banús Gómez and Camilo Zomeño López for their participation in the construction of the model and the performing of the test campaign. The authors would also express their thanks to Professor Angel Sanz-Andres, IDR/UPM Director, for his interest and his invaluable assistance on the elaboration of this work.

This work is part of the project TED2021-130541B-C21 funded by MCIN/AEI/10.13039/501100011033, the European Union "NextGenerationEU"/PRTR and project PID2022-137630OB-C21 financed by MCIN/AEI/10.13039/501100011033/FEDER, UE.

References

Andersen, M.S., Johansson, J., Brandt, A., Hansen, S.O., 2016. Aerodynamic stability of long span suspension bridges with low torsional natural frequencies. Eng. Struct. 120, 82–91. http://dx.doi.org/10.1016/j.engstruct.2016.04.025, URL: https://www.sciencedirect.com/science/article/pii/S0141029616301365.

Browne, M.T., Taylor, Z.J., Li, S., Gamble, S., 2020. A wind load design method for ground-mounted multi-row solar arrays based on a compilation of wind tunnel experiments. J. Wind Eng. Ind. Aerodyn. 205, 104294. http://dx.doi.org/10.1016/j.jweia.2020.104294, URL: https://www.sciencedirect.com/science/article/pii/S016761052030204X.

Cárdenas-Rondón, J.A., Franchini, S., Ogueta-Gutiérrez, M., Marín-Coca, S., Martínez-Cava, A., 2022. Experimental study of the relationship between the power spectral density of the incident wind and buffeting moment on a two-dimensional single-axis flat solar tracker. In: International Forum on Aerorelasticity and Structural Dynamics 2022. pp. 1–5.

Cárdenas-Rondón, J.A., Ogueta Gutiérrez, M., Franchini Longhi, S., 2019. Experimental study of the effect of the reduced frequency in the airfoil's aerodynamic characteristics. In: 8th European Conference for Aeronautics and Space Sciences. pp. 1–14.

Chen, Z., Shi, Z., Chen, S., Yao, Z., 2022. Stall flutter suppression of NACA 0012 airfoil based on steady blowing. J. Fluids Struct. 109, 103472. http://dx.doi.org/10.1016/j.jfluidstructs.2021.103472.

Cheruku, S., 2022. Wind-Induced Failures of Flexible Structures. In: Ninth Congress on Forensic Engineering. pp. 403–410.

Chowdhury, A.G., Sarkar, P.P., 2003. A new technique for identification of eighteen flutter derivatives using a three-degree-of-freedom section model. Eng. Struct. 25, 1763–1772.

Chowdhury, A.G., Sarkar, P.P., 2005. Experimental identification of rational function coefficients for time-domain flutter analysis. Eng. Struct. 27 (9), 1349–1364. http://dx.doi.org/10.1016/j.engstruct.2005.02.019, URL: https://www.sciencedirect.com/science/article/pii/S0141029605001355.

Diana, G., Rocchi, D., Argentini, T., 2013. An experimental validation of a band superposition model of the aerodynamic forces acting on multi-box deck sections. J. Wind Eng. Ind. Aerodyn. 113, 40–58. http://dx.doi.org/10.1016/j.jweia.2012.12.005, URL: https://www.sciencedirect.com/science/article/pii/S0167610512002863.

Duda, K., Magalas, L.B., Majewski, M., Zielinski, T.P., 2011. DFT-based estimation of damped oscillation parameters in low-frequency mechanical spectroscopy. IEEE Trans. Instrum. Meas. 60 (11), 3608–3618. http://dx.doi.org/10.1109/TIM.2011.2113124.

Gao, G., Zhu, L., Han, W., Li, J., 2018. Nonlinear post-flutter behavior and self-excited force model of a twin-side-girder bridge deck. J. Wind Eng. Ind. Aerodyn. 177, 227–241. http://dx.doi.org/10.1016/j.jweia.2017.12.007, URL: https://www.sciencedirect.com/science/article/pii/S0167610517306062.

Gao, G., Zhu, L., Øiseth, O., 2023. Nonlinear indicial functions for modelling aeroelastic forces of bluff bodies. http://dx.doi.org/10.21203/rs.3.rs-3132935/v1, PREPRINT (Version 1) available at Research Square.

Ghowdhury, A.G., Sarkar, P.P., 2003. A new technique for identification o eighteen flutter derivatives using a three-degree-of-frredom section model. Eng. Struct. 25, 1763–1772. http://dx.doi.org/10.1016/j.engstruct.2003.07.002.

Gifford, J., 2019. What broke at oakey. URL: https://www.pv-magazine-australia.com/2019/12/07/long-read-what-broke-at-oakey/. PV Magazine.

Gu, M., Zhang, R., Xiang, H., 2001. Parametric study on flutter derivatives of bridge decks. Eng. Struct. 23 (12), 1607–1613. http://dx.doi.org/10.1016/S0141-0296(01)00059-1, URL: https://www.sciencedirect.com/science/article/pii/S0141029601000591.

IRENA, 2022. Renewable power generation costs in 2021. p. 204, arXiv:arXiv:1011.1669v3. URL: https://www.irena.org/-/media/Files/IRENA/Agency/Publication/2018/Jan/IRENA_2017_Power_Costs_2018.pdf.

Jensen, A.G., 1997. Fluid dynamic derivatives: Marine and wind engineering approaches. J. Wind Eng. Ind. Aerodyn. 69–71, 777–793. http://dx.doi.org/10.1016/S0167-6105(97)00205-5, URL: https://www.sciencedirect.com/science/article/pii/S0167610597002055. Proceedings of the 3rd International Colloqium on Bluff Body Aerodynamics and Applications.

Li, N., Balas, M.J., Nikoueeyan, P., Yang, H., Naughton, J.W., 2016. Stall flutter control of a smart blade section undergoing asymmetric limit oscillations. Shock Vib. 2016, http://dx.doi.org/10.1155/2016/5096128.

Li, Z., Wu, B., Liao, H., Li, M., Wang, Q., Shen, H., 2022. Influence of the initial amplitude on the flutter performance of a 2D section and 3D full bridge with a streamlined box girder. J. Wind Eng. Ind. Aerodyn. 222, 104916. http://dx.doi.org/10.1016/j.jweia.2022.104916, URL: https://www.sciencedirect.com/science/article/pii/S0167610522000253.

Lopez-Nuñez, E., Ogueta-Gutiérrez, M., Manzanares-Bercial, R., Gómez-Ortega, O., Franchini, S., Roibás-Millán, E., Sanz-Andres, A., 2020. Aerodynamic instability of a hinged-deck cross-section cable-stayed bridge. J. Wind Eng. Ind. Aerodyn. 198, 104110. http://dx.doi.org/10.1016/j.jweia.2020.104110, URL: https://www.sciencedirect.com/science/article/pii/S0167610520300209.

Magalas, L.B., Malinowski, T., 2003. Measurement techniques of the logarithmic decrement. Solid State Phenomena 89, 247–260.

Martínez-García, E., Blanco-Marigorta, E., Gayo, J.P., Navarro-Manso, A., 2021. Influence of inertia and aspect ratio on the torsional galloping of single-axis solar trackers. Eng. Struct. 243, 112682. http://dx.doi.org/10.1016/J.ENGSTRUCT.2021.112682.

Martínez-García, E., Marigorta, E.B., Gayo, J.P., Navarro-Manso, A., 2021. Experimental determination of the resistance of a single-axis solar tracker to torsional galloping. Struct. Eng. Mech. 78 (5), 519–528. http://dx.doi.org/10.12989/sem.2021.78.5.519.

Meseguer-Ruiz, J., Sanz-Andrés, Á., Pindado-Carrión, S., Franchini, S., Alonso-Rodrigo, G., 2013. Aerodinámica Civil. Efectos Del Viento En Edificaciones Y Estructuras. Garceta, Madrid, Spain, p. 350.

Náprstek, J., Pospíšil, S., Hračov, S., 2007. Analytical and experimental modelling of non-linear aeroelastic effects on prismatic bodies. J. Wind Eng. Ind. Aerodyn. 95 (9), 1315–1328. http://dx.doi.org/10.1016/j.jweia.2007.02.022, URL: https://www.sciencedirect.com/science/article/pii/S0167610507000499.

Noda, M., Utsunomiya, H., Nagao, F., Kanda, M., Shiraishi, N., 2003. Effects of oscillation amplitude on aerodynamic derivatives. J. Wind Eng. Ind. Aerodyn. 91 (1), 101–111. http://dx.doi.org/10.1016/S0167-6105(02)00338-0, URL: https://www.sciencedirect.com/science/article/pii/S0167610502003380. Fifth Asia-Pacific Conference on Wind Engineering.

Reina, G.P., De Stefano, G., 2017. Computational evaluation of wind loads on sun-tracking ground-mounted photovoltaic panel arrays. J. Wind Eng. Ind. Aerodyn. 170, 283–293. http://dx.doi.org/10.1016/j.jweia.2017.09.002, URL: https://www.sciencedirect.com/science/article/pii/S0167610517303446.

Rohr, C., Bourke, P.A., Banks, D., 2015. Torsional Instability of Single-Axis Solar Tracking Systems. In: International Conference on Wind Engineering. Porto Alegre, Brazil, pp. 1–7.

Sarkar, P.P., Caracoglia, L., Haan, F.L., Sato, H., Murakoshi, J., 2009. Comparative and sensitivity study of flutter derivatives of selected bridge deck sections, part 1: Analysis of inter-laboratory experimental data. Eng. Struct. 31 (1), 158–169. http://dx.doi.org/10.1016/j.engstruct.2008.07.020, http://linkinghub.elsevier.com/retrieve/pii/S014102960800268Xhttp://www.sciencedirect.com/science/article/pii/S014102960800268X.

Sarkar, P.P., Jones, N.P., Scanlan, R.H., 1994. Identification of aeroelastic parameters of flexible bridges. J. Eng. Mech. 120 (8), 1718. http://dx.doi.org/10.1061/(ASCE)0733-9399(1994)120:8(1718).

Scanlan, R.H., Tomko, J.J., 1971. Airfoil and bridge deck flutter derivatives. J. Eng. Mech. 97, 1717–1737.

Simiu, E., Scanlan, R.H., 1996. Wind Effects on Structures. John Wiley and Sons, New York, USA, p. 688.

Sisto, F., 2015. A modern course in aeroelasticity. In: A Modern Course in Aeroelasticity: Fifth Revised and Enlarged Edition. Springer International Publishing, Cham, pp. 259–278. http://dx.doi.org/10.1007/978-3-319-09453-3_5.

Strømmen, E.N., 2010. Theory of Bridge Aerodynamics, second ed. Springer Berlin, Heidelberg, p. XXI, 302. http://dx.doi.org/10.1007/978-3-642-13660-3, URL: https://link.springer.com/book/10.1007/978-3-642-13660-3. Published: 01 July 2010.

Suárez, J.L., Cadenas, D., Rubio, H., Ouro, P., 2022. Vortex shedding dynamics behind a single solar PV panel over a range of tilt angles in uniform flow. Fluids 7 (10), 1–15. http://dx.doi.org/10.3390/fluids7100322.

Taylor, Z.J., Browne, M.T., 2020. Hybrid pressure integration and buffeting analysis for multi-row wind loading in an array of single-axis trackers. J. Wind Eng. Ind. Aerodyn. 197 (September 2019), 104056. http://dx.doi.org/10.1016/j.jweia.2019.104056.

Theodorsen, T., 1949. General Theory of Aerodynamic Instability and the Mechanism of Flutter. Technical Report.

Valentín, D., Valero, C., Egusquiza, M., Presas, A., 2022. Failure investigation of a solar tracker due to wind-induced torsional galloping. Eng. Fail. Anal. 135, 106137. http://dx.doi.org/10.1016/j.engfailanal.2022.106137, URL: https://www.sciencedirect.com/science/article/pii/S135063072200111X.

Xu, F., Ying, X., Zhang, Z., 2016. Effects of exponentially modified sinusoidal oscillation and amplitude on bridge deck flutter derivatives. J. Bridge Eng. 21 (5).

Zasso, A., 1996. Flutter derivatives: Advantages of a new representation convention. J. Wind Eng. Ind. Aerodyn. 60, 35–47. http://dx.doi.org/10.1016/0167-6105(96)00022-0, URL: https://www.sciencedirect.com/science/article/pii/0167610596000220. The Wind Engineering Society's 2nd UK Conference.

Zhang, X., Ma, W., Kang, X., Shao, Q., Tang, Z., 2023a. Experimental study of the torsional aeroelastic instability of single-axis solar trackers under different turbulence intensities. J. Wind Eng. Ind. Aerodyn. 240, 105486. http://dx.doi.org/10.1016/j.jweia.2023.105486, URL: https://www.sciencedirect.com/science/article/pii/S0167610523001897.

Zhang, X., Ma, W., Zhang, Z., Hu, L., Cui, Y., 2023b. Experimental study on the interference effect of the wind-induced large torsional vibration of single-axis solar tracker arrays. J. Wind Eng. Ind. Aerodyn. 240, 105470. http://dx.doi.org/10.1016/j.jweia.2023.105470, URL: https://www.sciencedirect.com/science/article/pii/S0167610523001733.